Coupling of Elastic Solids with Compressible Two-Phase Fluids for the Numerical Investigation of Cavitation Damaging[1]

Christian Dickopp[2], Roman Gartz[2], Siegfried Müller[2]

[2]*Institut für Geometrie und Praktische Mathematik, RWTH Aachen, Templergraben 55, 52056 Aachen, Germany*

dickopp@igpm.rwth-aachen.de,Roman.Gartz@web.de,mueller@igpm.rwth-aachen.de

Abstract

Cavitation damaging is investigated by simulation of the model problem of a single gas bubble in a compressible liquid collapsing near the surface of an elastic solid wall. The three-phase system is described by the compressible Euler equations supplemented by the stiffened gas law for both fluids, a non-conservative evolution equation for the gas fraction characterizing the liquid-gas interface and the elastodynamical equations for a linear-elastic solid. The fluid model and the solid model are coupled by transition conditions at the fluid-structure interface.

The fluid equations are discretized according to Saurel and Abgrall and for the elastodynamical equations a finite volume discretization is applied. These numerical methods are coupled by a weak coupling strategy. The numerical results exhibit von Schmidt waves in the structure as well as the fluid. As possible explanation for cavitation damaging the von Mises yield criterion is evaluated.

Key words : compressible two-phase flow, linear-elastic solid, weak coupling.

1 Introduction

The formation and collapse of vapor bubbles in a liquid is called cavitation. Although pressure waves emitted during the process of cavitation development and the collapse of cavities are known to damage adjacent solids — as was already conjectured by

[1]This work has been performed with funding of the German Research Council (DFG) by grant MU 1422/5-1.

Lord Rayleigh [58] — the mechanisms causing the damage of the solid are far from being completely understood.

Cavitation may be induced by a pressure drop in the liquid below vapor pressure due to local acceleration of the liquid flow. In this case, the liquid bursts at impurities or cavitation nuclei and creates a free surface filled with gas and/or vapor – the bubble. The composition of the bubble content depends on the previous situation of the liquid as well as the magnitude and the time scale for the pressure drop. Due to changes in the flow field, the pressure in the liquid surrounding the bubble may increase again causing its collapse. If the collapse takes place next to a surface of a solid structure, flow velocity and pressure fields become asymmetric and a liquid jet is developed either directed towards or away from the boundary, depending on the compliance of the solid as well as the stand off distance of the bubble. The processes taking place in the interior and exterior of the asymmetrically collapsing and oscillating bubble as well as the prediction of onset and extent of cavitation damage are still subject of theoretical and experimental research. However, the small time and space scales as well as the complicated, not fully clarified, dynamical processes pose a challenge for theoretical, numerical and experimental investigations. Especially advanced numerical investigations are needed to provide information about the radiated pressure wave, the jet and the highly transient flow phenomena in the fluid as well as the mechanical loadings of the structure surface initiating tension waves within the solid. Of particular interest are pressure and flow velocity fields in the liquid phase and shear stresses and deformation velocities inside the solid to clarify the question if breaking points are exceeded. Similarly, advanced experimental investigations are needed for comparisons.

Motivation The investigation of the dynamics of cavitation bubbles and their interaction with a compliant wall is of special interest in different real world applications arising, for instance, in engineering, medical applications and biology such as cavitation erosion of under water structures [52, 8, 56], lithotripsy and sonoporation [53, 54, 33], and cavitation–enhanced ablation of materials, e.g. biological tissues [13, 14]. In this context the investigation of the transient behavior of cavitation structures and their interaction with an adjacent elastic or elastic/plastic structure can be helpful to improve the resistibility of underwater structures such as ship propellers and ship walls against strong pressure waves or to optimize medical laser or lithotripter applications with regard to collateral damage to sensitive tissue structures in the vicinity of the laser focus or to its sonoporation capabilities for drug delivery.

In the past four decades, numerous experimental investigations with laser-induced cavitation bubbles have been performed. Recently, Lauterborn and Kurz [40] summarized the development of the experimental investigations in their extensive survey. Here we briefly sketch some of the results. For details we refer to [40] and the references listed therein: thanks to advanced measurement techniques, e.g. particle-based velocimetry [38] and shadowgraph or Schlieren imaging using high-speed cameras, new light was shed on the intricate interaction of a bubble with a neighboring boundary. Several effects have been observed in the collapse of a single, initially spherical bubble, such as the indentation of the bubble wall opposite to the solid surface and the development of a liquid jet directed towards the wall [52, 8, 39], the emis-

sion of pressure waves into the liquid when the bubble is collapsing, the generation of a counter-jet directed away from the structure [66], the formation of a vortex ring around the toroidal bubble developing after the jet penetration followed by the breakup of the toroidal bubble into a swarm of tiny bubbles that also emit waves when collapsing [63, 56] and bubble movement towards the wall caused by Bjerknes forces.

Although all these effects have been known for a long time now, their influence on cavitation erosion is still under discussion. One problem is the lack of measurement data that typically are available at very few isolated points only which can be reached by measurement techniques without disturbing the dynamical processes. Informations concerning the transient behavior of the content of the bubble is not directly accessible. Pressure and temperature distributions can only be estimated by analyzing the sound and light emission into the liquid phase.

By dynamical comparison of experimentally observed phenomena only conjectures can be made based on the causal connection. Here numerical simulations of the bubble–boundary interaction could yield a valuable contribution to a better understanding of the complicated dynamics by providing pressure contours and velocity vectors in the liquid surrounding the bubble which are not easily accessible by experiments, and also providing information on the gas state. However, many of the numerical results obtained within the last four decades have been based on strongly simplifying models only, as typically assuming incompressibility of the liquid and neglecting viscosity and heat conduction effects. Even nowadays the bubble dynamics is frequently modeled using potential flow [9], where the gas state is not described by dynamic equations but is assumed to be spatially constant, or a homogeneous pressure state is assumed that is inserted into the dynamic conditions at the bubble wall. To solve the equations of potential flow, typically the boundary integral method is used because of its high performance which is very appealing with respect to computational aspects. So on one hand this approach formed an applicable way to simulate relevant time scales for the very transient processes but on the other hand it cannot be extended to more realistic flow descriptions because of mathematical limitations of the potential ansatz.

Sharp Interface Model. Due to the development of more advanced numerical concepts and more powerful computer hardware, attempts have been made during the past two decades to take into account the compressibility of both the liquid and the gas phase as well as the dynamical changes of the gas inside the bubble [70, 18, 64, 67, 51]. For this purpose, systems of balance equations have to be formulated for both phases supplemented by material laws. The two phases are coupled at the phase interface via jump conditions.

For the numerical simulation of two–phase immiscible flows in compressible fluids, the literature distinguishes between the Lagrangian and the Eulerian approach. The Lagrangian framework is characterized by a tracking ansatz for the interface during the time evolution. There are mainly three types of such techniques: (i) particle methods, e.g., Smooth Particle Hydrodynamics, where the movement of particles is simulated [47, 22], (ii) front tracking methods where the underlying discretization undergoes a deformation due to the movement of the interface [32, 15, 37], and (iii) marker methods, e.g., Marker and Cells [69], Volume of Fluid [29], where the dis-

cretization is fixed. Typically difficulties arise for complicated topological changes of the interface. To overcome this obstacle techniques have been developed based on an Eulerian formulation, i.e., the interface is captured. To distinguish the two fluid phases within this formulation the underlying equations of motion are supplemented with an additional scalar equation indicating the position of the interface and spatial distribution of the both phases, for instance, a color function [12] or a level set function [55, 62]. In the past decade several numerical schemes have been proposed in the literature based on this idea, for instance, the level set method [48], the hybrid multifluid method [35], the non-conservative scheme of Saurel and Abgrall [61], the Ghost Fluid Method [25, 68, 24], the two-flux method [3, 2] and the Lagrange-projection scheme [5].

Recent investigations [4, 5] show that not all of these approaches are useful for the numerical investigation of the collapse of a single laser-induced cavitation bubble. The reason for this might be the challenges imposed by the problem: due to bubble oscillations the bubble radius may vary by several orders of magnitude. Instabilities at the bubble interface occur because of the tremendous change of acoustic impedance. Moreover, the interface velocity may become supersonic in the bubble collapse which causes very small time steps. Therefore the numerical simulation of these problems can only be performed using robust and efficient schemes that allow for very high resolution in space and time to obtain sufficient accuracy.

Fluid-Structure Interaction. So far, the dynamic processes inside the solid have been investigated mathematically and numerically only by a few groups. However, the investigation of the transient distribution of stresses is important to understand the cause of the observed damaging by comparisons with breaking points of the material. In order to investigate numerically cavitation erosion, the model of immiscible, two-phase compressible fluids has to be coupled with a model for elastic or elastic/plastic solids. In this regard, only few results are reported in the literature. Duncan and Zhang [23] model the elastic solid by a membrane that is based on springs. The results show a significant influence of the dynamic processes inside the solid on the cavitation problem. In [34] the dynamic behavior of all three phases is investigated. The authors couple in an alternating way a boundary integral method approximating the solution for a potential ansatz for both fluids under simplifying assumptions with an implicit finite element method to determine the stresses and velocities inside the solid. For axial rotational symmetry Dickopp [18] developed an explicit finite element Galerkin scheme with flux-corrected transport for the solution of the Euler/Navier-Stokes equations in two space dimensions and time on unstructured grids. Here surface tension is taken into account, evaporation and condensation are neglected. The material interface is considered a sharp interface that is fitted, i.e., it coincides with a line of a moving mesh. By means of this solver wave processes at an early stage in a three-phase system have been investigated [19, 20, 7, 21]. In [64] the interaction between the fluids and an elastic-plastic solid is numerically investigated. For this purpose an algorithm is developed to couple two existing codes solving the Navier-Stokes equations for compressible fluids and the equations for the dynamics of elastic-plastic solids.

More recently there have been numerical investigations performed by Turangan et al. [65]. Simulations are conducted for a bubble near an aluminum layer with

planar and notched surfaces, respectively, using a free-Lagrange numerical method on Voronoi meshes coupled to an elastic-perfectly plastic material model using the method of radial return. In all simulations using a planar solid surface the aluminum layers are still in the elastic regime, i.e., material damage observed in experiments [56] could not yet be confirmed numerically. Only for notched surfaces evidence for material damage could be found applying a yield criterion to the data in a post-processing step.

Outline. In Section 2 we summarize the governing equations for a compressible two-phase flow and a linear-elastic solid. These form two hyperbolic systems of conservation laws and a non-conservative evolution equation for the gas fraction characterizing the liquid-gas interface that are coupled by transition conditions at the fluid-structure interface. The hyperbolic systems are discretized by finite volume schemes and a non-conservative upwind discretization is applied to the evolution equations for the gas fraction. The discretizations for the fluid and the structure are coupled by a weak coupling strategy that is described in Section 3. The resulting scheme is then applied to the numerical simulation of a collapsing spherical bubble next to a planar elastic wall. In Section 4 we discuss two issues, namely, (i) von Schmidt waves that occur in the structure as well as in the fluid due to the fluid-structure interaction and (ii) cavitation damaging characterized by the von Mises yield condition.

2 Mathematical Models

In this section the governing equations modeling a compressible two-phase fluid and an elastic solid are summarized, namely, the Navier-Stokes equations and the linear elastodynamical equations, respectively. Neglecting viscosity and heat conduction in the fluid and displacements of the structure these systems are hyperbolic and can be written in conservative form. They are coupled at the fluid-structure interface by transition conditions. The liquid-gas interface is characterized by the gas fraction that is evolved in time by a non-conservative upwind discretization.

2.1 Two-phase Fluid Model

The two-phase flow is modeled by the compressible Navier–Stokes equations using the ansatz of a sharp interface Γ separating the liquid phase and the gas phase

$$\frac{\partial}{\partial t}\rho + \operatorname{div}(\rho\,\mathbf{v}) = \delta_{\Gamma,\varepsilon}(d)\,\dot{\mathbf{m}}^T\,\mathbf{n}_\Gamma, \tag{1}$$

$$\frac{\partial}{\partial t}(\rho\,\mathbf{v}) + \operatorname{div}(\rho\,\mathbf{v}^T\,\mathbf{v} + p\,\mathbf{I}) = \operatorname{div}(\boldsymbol{\tau}_v) + \delta_{\Gamma,\varepsilon}(d)\,\gamma\,\boldsymbol{\kappa}\,\mathbf{n}_\Gamma, \tag{2}$$

$$\frac{\partial}{\partial t}(\rho\,E) + \operatorname{div}(\rho\,\mathbf{v}\,(E + p/\rho)) = \operatorname{div}(\boldsymbol{\tau}_v\,\mathbf{v} - \mathbf{q}) + \delta_{\Gamma,\varepsilon}(d)\,(\gamma\,\boldsymbol{\kappa}\,\mathbf{v}^T + \mathbf{q}_{lat}^T)\,\mathbf{n}_\Gamma \tag{3}$$

using mass density ρ, momentum $\rho\,\mathbf{v}$ and total energy $\rho\,E$. Here p, $\boldsymbol{\tau}_v$ and $\mathbf{q}$ denote the pressure, the tensor of deviatoric stresses and the heat flux, respectively. Furthermore, γ is the surface tension, $\boldsymbol{\kappa}$ the mean curvature of the interface that reads $\boldsymbol{\kappa} = r^{-1}\mathbf{I}$ in the special case of a sphere, d the normal distance to the front, $\delta_{\Gamma,\varepsilon}$

a smoothed Dirac delta function and $\mathbf{n}_\Gamma$ the unit outward normal vector at the front. The surface tension term is considered to be a force concentrated on the interface. Optionally applied models for condensation and evaporation at the bubble interface describe the mass flow rate $\dot{\mathbf{m}}$ as an additional transient variable along the phase interface. In case of such mass exchanges between the liquid and the gas also an energy transfer between the two phases is caused that has to be taken into account in the energy balance by the so-called latent heat flow $\mathbf{q}_{lat} = L\,\dot{\mathbf{m}}$, where L denotes the latent heat. Since our interest is in bubbles with a small diameter, we neglect effects of gravity.

The smoothed Dirac delta function $\delta_{\Gamma,\varepsilon}$ is unity inside a layer of thickness ε near to the interface Γ and vanishes outside a 2ε-layer blending smoothly between the layer and the far field. Typically ε is chosen proportional to the discretization, i.e., $\delta_{\Gamma,\varepsilon}$ tends to the Dirac delta function δ_0 in the limit. Due to the finite thickness of the layer the continuum mechanical jump conditions at the phase interface can be derived as a contact discontinuity with a change of the material:

$$\begin{aligned}
&[\rho\, v] = \dot{\mathbf{m}}^T\, \mathbf{n}_\Gamma,\\
&[\rho\, \mathbf{v}\, v + (p\, \mathbf{I} - \boldsymbol{\tau}_v)\, \mathbf{n}_\Gamma] = \gamma\, \boldsymbol{\kappa}\, \mathbf{n}_\Gamma,\\
&[\rho\, E\, v + \left(\mathbf{v}^T\, (p\, \mathbf{I} - \boldsymbol{\tau}_v) + \mathbf{q}^T\right)\, \mathbf{n}_\Gamma] = (\gamma\, \boldsymbol{\kappa}\, \mathbf{v}^T + \mathbf{q}_{lat}^T)\, \mathbf{n}_\Gamma,
\end{aligned} \tag{4}$$

where $[f] := f_{liquid} - f_{gas}$ denotes the jump of a quantity f across the interface. The normal component of the relative velocity at the interface is determined by $v = (\mathbf{v} - \mathbf{v}_\Gamma)^T\, \mathbf{n}_\Gamma$ with $\mathbf{v}_\Gamma$ the interfacial velocity. Assuming that the mass of the gas phase is negligibly small in comparison to the mass of the liquid, we deduce from the first jump relation in equation (4) for the normal component

$$\mathbf{v}_\Gamma\, \mathbf{n}_\Gamma^T = \mathbf{v}\, \mathbf{n}_\Gamma^T + \dot{\mathbf{m}}^T\, \mathbf{n}_\Gamma / \rho_{liquid}, \tag{5}$$

The system (1)-(3) has to be closed by a pressure law. In this work, we consider the stiffened gas law suggested in [1, 16]. It reads

$$p(\rho, e, \varphi) = (\gamma(\varphi) - 1)\rho e - \gamma(\varphi)\pi(\varphi), \tag{6}$$

where the two phases (here gas and liquid) are distinguished by an additional field variable φ. Observe that with $\pi = 0$ a standard perfect gas law is recovered. In a similar way, the material parameters of the two phases are distinguished.

In Section 4 we are interested in the collapse of a laser-induced cavitation bubble near to an elastic solid. Therefore the flow model (1)-(3) is further simplified: surface tension and phase transition may become important when the bubble reaches its minimum size in the collapse. However the collapse time is very short. Hence, these effects are assumed to have only a small influence. For the surface tension this was investigated in [51] for a cylindrical bubble. Furthermore viscosity and heat conduction are neglected. These dissipative effects only affect the states in the instant of shock focusing in the bubble center according to Guderley's similarity solution for spherical compression waves, cf. [26], but merely little effects on the bubble collapse are expected based on previous investigations in [27]. Viscosity might be significant for the collapse of large bubbles as has been verified by numerical studies in [57], where thermal effects on the bubble rebound are discussed.

Moreover, in Section 4 the assumption of axial symmetry is reasonable for the investigated problem of a collapsing single spherical bubble next to an elastic solid. Therefore the system of governing equations is transformed from Euclidean to cylindrical coordinates r, z and ϕ. Because of the axial symmetry all partial derivatives with respect to the angle coordinate ϕ vanish. Due to the coordinate transformation Christoffel symbols are introduced resulting in a geometrical source term. Then the quasi–two–dimensional formulation of the compressible two-phase Euler equations reads:

$$\frac{\partial}{\partial t}(r\,\mathbf{U}) + \frac{\partial}{\partial z}(r\,\mathbf{F}_z(\mathbf{U})) + \frac{\partial}{\partial r}(r\,\mathbf{F}_r(\mathbf{U})) = \mathbf{S}(\mathbf{U}) \tag{7}$$

with

$$\mathbf{U} = \begin{pmatrix} \rho \\ \rho v_z \\ \rho v_r \\ \rho E \end{pmatrix},\ \mathbf{F}_z = \begin{pmatrix} \rho v_z \\ \rho v_z^2 + p \\ \rho v_z v_r \\ v_z(\rho E + p) \end{pmatrix},\ \mathbf{F}_r = \begin{pmatrix} \rho v_r \\ \rho v_r v_z \\ \rho v_r^2 + p \\ v_r(\rho E + p) \end{pmatrix},\ \mathbf{S} = \begin{pmatrix} 0 \\ 0 \\ p \\ 0 \end{pmatrix}. \tag{8}$$

2.1.1 Evolution of phase boundary by gas fraction

In the following the phase indicator φ is identified with the gas fraction. We define that $\varphi = 0$ and $\varphi = 1$ correspond to pure liquid and pure gas, respectively. Since we are interested in very high speed flows and very short observation times, phase transition is neglected, i.e., there is no mass transfer between the two fluids. Thus the gas fraction obeys a homogeneous transport equation, i.e., its material derivative vanishes,

$$\frac{D\,\varphi}{D\,t} = \frac{\partial\,\varphi}{\partial\,t} + v_z\,\frac{\partial\,\varphi}{\partial\,z} + v_r\,\frac{\partial\,\varphi}{\partial\,r} = 0. \tag{9}$$

If at initial time $t = 0$ the fraction φ takes only the values 0 or 1 characterizing the bubble shape, it will retain its value for $t > 0$. Thus there is no physical mixing in the continuous model. However, the numerical model will introduce artificial mixture zones where $0 < \varphi < 1$ leading to some difficulties which are discussed in [50, 51].

To study only the continuous model, it would be sufficient to provide the values of the material parameters γ and π for $\varphi = 0$ or $\varphi = 1$ in the pressure law (6). But because of the numerical mixture, it is necessary to interpolate γ and π for $0 < \varphi < 1$. An arbitrary choice of interpolation would lead to numerical difficulties that are studied in many works, see for instance [1]. A linear interpolation of the parameters $\beta_1 = 1/(\gamma-1)$ and $\beta_2 = \gamma\pi/(\gamma-1)$ has been found to be a useful ansatz, i.e.,

$$\beta_1(\varphi) = \varphi\beta_1(1) + (1-\varphi)\beta_1(0), \quad \beta_2(\varphi) = \varphi\beta_2(1) + (1-\varphi)\beta_2(0). \tag{10}$$

The mixture pressure law coefficients $\gamma(\varphi)$ and $\pi(\varphi)$ are then obtained from the reverse relation, i.e.,

$$\gamma(\varphi) = 1 + 1/\beta_1(\varphi), \quad \pi = \beta_2(\varphi)/(1 + \beta_1(\varphi)). \tag{11}$$

For pure water and air the material parameters γ and π are listed in Table 1. Here the minimal pressure for the pure liquid is deduced from the speed of sound

		Gas	Liquid
γ	-	1.4	7.15
π	Pa	0	3×10^8

Table 1: Material coefficients.

$c^2 = \gamma\,(p+\pi)/\rho$, where we choose $c_l = 1500$ m/s, $\gamma_l = 1.1$, $\rho_l = 1000$ kg/m^3 and $p_l = 10^5$ Pa. Usually in the stiffened gas model for a liquid, higher values of γ_l are proposed as in [16]. However, smaller values for γ_l result in a higher minimal pressure π_l and, hence, the variation of the sound speed in the liquid is smaller.

2.2 Linear Elastic Solid Model

The structure model can be derived from the continuum mechanical conservation principles for densities of mass, momentum, angular momentum and energy of a solid. Assuming symmetry of the stress tensor the balance of the angular momentum is equivalent to the conservation of momentum. Because of the very short observation times in the experiments of laser-induced cavitation bubbles, the solid temperature remains constant and, hence, the heat flux is negligible. Therefore the balance of energy decouples from the other conservation laws and has not to be taken into account to describe the mechanical behavior of the structure as explained in the following. This simplification does not influence the flow of the adjacent liquid, although the fluid and the solid are coupled at the fluid-structure interface by the jump conditions for contact discontinuities, see Section 2.3: the conservation of energy at the fluid-structure interface leads to an equation containing the jump of the heat fluxes and the shear stresses acting in normal direction to the contact line. Therefore the temperature does not arise explicitly within the solid side of the jump relation but only by the heat flux. Since the heat flux is neglected, the temperature of the structure merely arises in the energy balance in this media without any coupling to the other equations of the system, i.e., the temperature as well as the energy balance have not to be taken into account within the solid to obtain a closed system of equations.

Furthermore, as a consequence of the arrangement of the molecules in the shape of a crystal grid, solid materials are characterized by the fact that variations of the density are essentially smaller than within a fluid. Therefore the mass balance is neglected and a constant solid density is inserted into the momentum equation considered in the following:

Thus the system of conservation laws for the structure reduces to Newton's law in its general formulation:

$$\frac{D\overline{\rho}\overline{\mathbf{v}}}{Dt} = \operatorname{div}\overline{\boldsymbol{\sigma}}, \tag{12}$$

with $\overline{\rho}$ the density of the solid, $\overline{\boldsymbol{\sigma}}$ the shear stress tensor in the solid and $\overline{\mathbf{v}} := \partial\,\overline{\mathbf{u}}/\partial\,t$ the deformation velocity defined by the displacement vector $\overline{\mathbf{u}}$. The material derivative of some quantity f is defined as

$$\frac{Df}{Dt} := \frac{\partial\,f}{\partial\,t} + \overline{\mathbf{v}}^T \cdot \nabla f. \tag{13}$$

Note that we distinguish the variables of the solid from their counterparts in the fluid by a bar. The absolute values of the deformation velocities are supposed to be so small such that the material derivatives may be approximated by partial time derivatives, i.e., we may neglect displacements of the structure:

$$\frac{D\,f}{D\,t} \approx \frac{\partial\,f}{\partial\,t}. \tag{14}$$

Thus, with a constant density, the momentum equation (12) simplifies to

$$\overline{\rho}\,\frac{\partial\,\overline{\mathbf{v}}}{\partial\,t} = \operatorname{div}\overline{\boldsymbol{\sigma}}. \tag{15}$$

In order to close equation (15), we have to provide an equation for the stress tensor. Assumptions concerning symmetry, homogeneity and isotropy of the structure behavior allow to reduce the original 81 components of the common continuum mechanical ansatz for the nine components of the stress tensor as linear functions of the nine components of the strain tensor. Hooke's linear ansatz for the relation between the stress tensor and the deformation tensor states a reasonable model for an elastic behavior of a homogeneous and isotropic material under the assumption of small deformations:

$$d\,\overline{\boldsymbol{\sigma}} = \overline{\lambda}\,\mathrm{tr}(d\,\overline{\boldsymbol{\varepsilon}})\,\mathbf{I} + 2\,\overline{\mu}\,d\,\overline{\boldsymbol{\varepsilon}} \tag{16}$$

using the trace operator tr. It characterizes the material behavior under loadings by the two Lamé-coefficients $\overline{\lambda}$ and $\overline{\mu}$ related to Poisson's ratio and the strain tensor $\overline{\boldsymbol{\varepsilon}} = \frac{1}{2}(\nabla\,\overline{\mathbf{u}} + (\nabla\,\overline{\mathbf{u}})^T)$. For small deformations as assumed here and neglecting plastic deformation, a geometrical linearization neglects quadratic or higher order terms of the deformation gradient in the equation for the strain tensor, i.e., we assume a linear elastic material behavior. Then the strains are linear functions of the gradient of the deformation velocities, i.e., $d\,\overline{\boldsymbol{\varepsilon}} = \overline{\boldsymbol{\varepsilon}}$ and $\mathrm{tr}(\frac{\partial\overline{\boldsymbol{\varepsilon}}}{\partial t})\,\mathbf{I} = \operatorname{div}\overline{\mathbf{v}}\,\mathbf{I}$ in (16), resulting in Hooke's law as a linear stress-strain relation. Differentiation of Hooke's law with respect to time then provides

$$\frac{\partial\,\overline{\boldsymbol{\sigma}}}{\partial\,t} = \overline{\lambda}\operatorname{div}(\overline{\mathbf{v}})\,\mathbf{I} + \overline{\mu}\,\left(\nabla\,(\overline{\mathbf{v}}) + (\nabla\,(\overline{\mathbf{v}}))^T\right). \tag{17}$$

The equations (15) and (17) form a system of linear, hyperbolic differential equations of first order for the deformation velocities $\overline{\mathbf{v}}$ and the components of the stress tensor $\overline{\boldsymbol{\sigma}}$ that can be written in divergence form

$$\frac{\partial\,\overline{\mathbf{U}}}{\partial\,t} = \operatorname{div}\left(\overline{\mathbf{F}}_x(\overline{\mathbf{U}}), \overline{\mathbf{F}}_y(\overline{\mathbf{U}}), \overline{\mathbf{F}}_z(\overline{\mathbf{U}})\right) \tag{18}$$

with

$$\overline{\mathbf{U}} = \begin{pmatrix} \overline{v}_x \\ \overline{v}_y \\ \overline{v}_z \\ \overline{\sigma}_{xx} \\ \overline{\sigma}_{yy} \\ \overline{\sigma}_{zz} \\ \overline{\sigma}_{xy} \\ \overline{\sigma}_{xz} \\ \overline{\sigma}_{yz} \end{pmatrix}, \overline{\mathbf{F}}_x = \begin{pmatrix} \overline{\sigma}_{xx}/\overline{\rho} \\ \overline{\sigma}_{xy}/\overline{\rho} \\ \overline{\sigma}_{xz}/\overline{\rho} \\ \overline{\rho}\,c_1^2\,\overline{v}_x \\ \overline{\rho}\,c_1^2\,\alpha\,\overline{v}_x \\ \overline{\rho}\,c_1^2\,\alpha\,\overline{v}_x \\ \overline{\rho}\,c_2^2\,\overline{v}_y \\ \overline{\rho}\,c_2^2\,\overline{v}_z \\ 0 \end{pmatrix}, \overline{\mathbf{F}}_y = \begin{pmatrix} \overline{\sigma}_{xy}/\overline{\rho} \\ \overline{\sigma}_{yy}/\overline{\rho} \\ \overline{\sigma}_{yz}/\overline{\rho} \\ \overline{\rho}\,c_1^2\,\alpha\,\overline{v}_y \\ \overline{\rho}\,c_1^2\,\overline{v}_y \\ \overline{\rho}\,c_1^2\,\alpha\,\overline{v}_y \\ \overline{\rho}\,c_2^2\,\overline{v}_x \\ 0 \\ \overline{\rho}\,c_2^2\,\overline{v}_z \end{pmatrix}, \overline{\mathbf{F}}_z = \begin{pmatrix} \overline{\sigma}_{xz}/\overline{\rho} \\ \overline{\sigma}_{yz}/\overline{\rho} \\ \overline{\sigma}_{zz}/\overline{\rho} \\ \overline{\rho}\,c_1^2\,\alpha\,\overline{v}_z \\ \overline{\rho}\,c_1^2\,\alpha\,\overline{v}_z \\ \overline{\rho}\,c_1^2\,\overline{v}_z \\ 0 \\ \overline{\rho}\,c_2^2\,\overline{v}_x \\ \overline{\rho}\,c_2^2\,\overline{v}_y \end{pmatrix}.$$

Herein, the coefficients c_1^2 and c_2^2 denote the squares of the dilatation wave velocity and the shear wave velocity, respectively,

$$c_1^2 = \frac{\overline{\lambda} + 2\,\overline{\mu}}{\overline{\rho}}, \quad c_2^2 = \frac{\overline{\mu}}{\overline{\rho}} \quad \text{and} \quad \alpha = 1 - 2\left(\frac{c_2}{c_1}\right)^2.$$

In view of Section 4, where we consider an axial symmetric problem, we rewrite (15) in cylindrical coordinates where we neglect all derivatives with respect to the angular coordinate ϕ. The linear system of elastodynamical equations in quasi-2D then reads

$$\frac{\partial}{\partial t}(r\,\overline{\mathbf{U}}) = \frac{\partial}{\partial z}(r\,\overline{\mathbf{F}}_z(\overline{\mathbf{U}})) + \frac{\partial}{\partial r}(r\,\overline{\mathbf{F}}_r(\overline{\mathbf{U}})) + \overline{\mathbf{S}}(\overline{\mathbf{U}}) \tag{19}$$

with

$$\overline{\mathbf{U}} = \begin{pmatrix} \overline{v}_z \\ \overline{v}_r \\ \overline{\sigma}_{zz}/\overline{\rho}c_2^2 \\ \overline{\sigma}_{zr}/\overline{\rho}c_2^2 \\ \overline{\sigma}_{rr}/\overline{\rho}c_2^2 \\ \overline{\sigma}_{\phi\phi}/\overline{\rho}c_2^2 \end{pmatrix}, \; \overline{\mathbf{F}}_z = \begin{pmatrix} \overline{\sigma}_{zz}/\overline{\rho} \\ \overline{\sigma}_{zr}/\overline{\rho} \\ \overline{v}_z \\ \overline{v}_r \\ \alpha\overline{v}_z \\ \alpha\overline{v}_z \end{pmatrix}, \; \overline{\mathbf{F}}_r = \begin{pmatrix} \overline{\sigma}_{zr}/\overline{\rho} \\ \overline{\sigma}_{rr}/\overline{\rho} \\ \alpha\overline{v}_r \\ \overline{v}_z \\ \overline{v}_r \\ \alpha\overline{v}_r \end{pmatrix}, \; \overline{\mathbf{S}} = \begin{pmatrix} 0 \\ -\overline{\rho}/\overline{\sigma}_{\phi\phi} \\ 0 \\ -\overline{v}_z \\ (\alpha-1)\overline{v}_r \\ (1-\alpha)\overline{v}_r \end{pmatrix}. \tag{20}$$

2.3 Transition Conditions at the Fluid-Structure Interface

At the fluid-structure interface $\overline{\Gamma}$ the fluid state $\mathbf{U}$ and the solid state $\overline{\mathbf{U}}$ are coupled by transition conditions and kinematic conditions according to (4). These coincide with the jump conditions for a contact discontinuity that are derived in continuum mechanics. In case of a viscous flow neglecting phase transition and surface tension these read

$$-p + \mathbf{n}_{\overline{\Gamma}}^T\,\boldsymbol{\tau}_v\,\mathbf{n}_{\overline{\Gamma}} = \mathbf{n}_{\overline{\Gamma}}^T\,\overline{\boldsymbol{\sigma}}\,\mathbf{n}_{\overline{\Gamma}}, \quad \mathbf{n}_{\overline{\Gamma}}^T\,\boldsymbol{\tau}_v\,\mathbf{t}_{\overline{\Gamma}} = \mathbf{n}_{\overline{\Gamma}}^T\,\overline{\boldsymbol{\sigma}}\,\mathbf{t}_{\overline{\Gamma}}, \quad \mathbf{v} = \overline{\mathbf{v}}. \tag{21}$$

Here $\mathbf{n}_{\overline{\Gamma}}$ and $\mathbf{t}_{\overline{\Gamma}}$ denote the normal and tangential vector with respect to the material interface $\overline{\Gamma}$. Neglecting viscous effects in the fluid, i.e., $\boldsymbol{\tau}_v = \mathbf{0}$, they simplify to

$$-p = \mathbf{n}_{\overline{\Gamma}}^T\,\overline{\boldsymbol{\sigma}}\,\mathbf{n}_{\overline{\Gamma}}, \quad \mathbf{v}^T\mathbf{n}_{\overline{\Gamma}} = \overline{\mathbf{v}}^T\mathbf{n}_{\overline{\Gamma}}. \tag{22}$$

3 Numerical Discretization

Both systems of equations (7) and (19) are discretized by finite volume schemes. For the evolution equation (9) of the gas fraction a non-conservative upwind discretization is used. The fluid-structure coupling is realized by a weak coupling strategy, where the transition conditions are split into two conditions that are used as boundary conditions for the fluid and the structure, respectively.

3.1 Finite Volume Discretization of Fluid and Structure Equations

Since both systems of equations (7) and (19) for the fluid and for the solid, respectively, are given in conservative form, finite volume schemes are applied to discretize these equations. For a structured grid in a two-dimensional spatial space with coordinates z and r, i.e., $V_{ij} = [z_{i-\frac{1}{2}}, z_{i+\frac{1}{2}}] \times [r_{j-\frac{1}{2}}, r_{j+\frac{1}{2}}]$, these discretizations can be written as

$$\begin{aligned} \mathbf{v}_{ij}^{n+1} = \mathbf{v}_{ij}^{n} \quad &- \quad \frac{\Delta t}{\|V_{ij}\|} \left(\|\Gamma_{z,i+\frac{1}{2},j}\| \mathbf{G}^{n}_{z,i+\frac{1}{2},j} - \|\Gamma_{z,i-\frac{1}{2},j}\| \mathbf{G}^{n}_{z,i-\frac{1}{2},j} \right) \\ &- \quad \frac{\Delta t}{\|V_{ij}\|} \left(\|\Gamma_{r,i,j+\frac{1}{2}}\| \mathbf{G}^{n}_{r,i,j+\frac{1}{2}} - \|\Gamma_{r,i,j-\frac{1}{2}}\| \mathbf{G}^{n}_{r,i,j-\frac{1}{2}} \right) + \frac{\Delta t |V_{ij}|}{\|V_{ij}\|} \mathbf{S}^{n}_{ij} \end{aligned} \tag{23}$$

with the volumes $|V_{ij}| := \Delta z_i \, \Delta r_j = (z_{i+\frac{1}{2}} - z_{i-\frac{1}{2}}) \, (r_{j+\frac{1}{2}} - r_{j-\frac{1}{2}})$, $\|V_{ij}\| := r_j \Delta r_j \Delta z_i$, $r_j := \left(r_{j+\frac{1}{2}} + r_{j-\frac{1}{2}} \right) / 2$ and the interface areas $\|\Gamma_{r,i,j\pm\frac{1}{2}}\| := \Delta z_i \, r_{j\pm\frac{1}{2}}$, $\|\Gamma_{z,i\pm\frac{1}{2},j}\| := r_j \, \Delta r_j$. For a detailed derivation we refer to [4], Appendix A.

Here $\mathbf{v}_{ij}^{n}$ denotes an approximation of $\mathbf{U}$ and $\overline{\mathbf{U}}$ in the cell V_{ij} using numerical fluxes $\mathbf{G}_z$, $\mathbf{G}_r$ and $\overline{\mathbf{G}}_z$, $\overline{\mathbf{G}}_r$ as well as numerical source terms $\mathbf{S}$ and $\overline{\mathbf{S}}$ corresponding to either the fluid or the solid, respectively. The numerical source terms are approximated by an average over the cell that can be located in its center.

The numerical fluxes are determined by solving Riemann problems at the cell interfaces. For the approximation of the solution of the flow problem the exact solver following Colella and Glaz [17] is applied, whereas the Riemann solution of the solid equations is determined by Roe's solver [59] that is exact for the linear system of equations. The spatial accuracy is improved by a quasi-one-dimensional polynomial reconstruction. For this purpose we apply a linear ENO reconstruction in each coordinate direction, cf. [28]. For a non-uniform grid this reads for the left and the right state of the Riemann problem:

$$\mathbf{v}_k^L = \mathbf{v}_{k-1} + (h_{k-1} \, \mathbf{I} - \tau \, \mathbf{A}_{k-1}) \, \overline{m} \, (\Delta \, \mathbf{v}_{k-1}, \Delta \, \mathbf{v}_k) \, , \tag{24}$$

$$\mathbf{v}_k^R = \mathbf{v}_k - (h_k \, \mathbf{I} + \tau \, \mathbf{A}_k) \, \overline{m} \, (\Delta \, \mathbf{v}_k, \Delta \, \mathbf{v}_{k+1}) \tag{25}$$

using the divided differences $\Delta \, \mathbf{v}_i := (\mathbf{v}_i - \mathbf{v}_{i-1})/(h_i + h_{i-1})$ and the minmod function $\overline{m}$ componentwise defined by $\overline{m}(a, b) := a$ if $|a| \leq |b|$ and $\overline{m}(a, b) := b$ elsewhere. Note that the term corresponding to the time discretization τ ensures second order accuracy in time. The reconstruction technique is either applied to the primitive variables and the gas fraction $(\rho, v_z, v_r, p, \varphi)^T$ or to the quantities $(\overline{v}_z, \overline{v}_r, \overline{\sigma}_{rr}, \overline{\sigma}_{rz}, \overline{\sigma}_{zz}, \overline{\sigma}_{\phi\phi})^T$ in case of the fluid equations and the solid equations, respectively. Thus the matrix $\mathbf{A}$ in (24) corresponds either to the matrix of (7) written in quasi-conservative form or to the Jacobian of the fluxes in (19) in z- or r-direction, respectively.

Note that it is convenient to reconstruct pressure and velocity rather than some other thermodynamical variable because this will preserve homogeneous pressure and velocity fields. According to the Saurel-Abgrall trick [60] this is essential to ensure stability of the discretization at the phase boundary.

Finally the efficiency of these discretizations is enhanced by applying multiscale-based grid adaptation techniques, cf. [49, 51].

3.2 Upwind Discretization of Gas Fraction

The quantity $r\,\rho\,\varphi$ satisfies the conservative equation

$$\frac{\partial}{\partial t}(r\,\rho\,\varphi) + \frac{\partial}{\partial z}(r(\rho\,v_z\,\varphi)) + \frac{\partial}{\partial r}(r(\rho\,v_r\,\varphi)) = 0 \tag{26}$$

due to the mass conservation in (7) and the gas fraction evolution equation (9). Typically the discretization of this conservative equation leads to instabilities that will cause the breakdown of the computation, whereas the non-conservative discretization suggested by Saurel and Abgrall leads to successful computations, cf. [1, 60]. However a rigorous mathematical justification of this practical fact is still missing even in the Cartesian case.

The Saurel-Abgrall approach consists in imposing that the scheme preserves a constant pressure and velocity field, i.e., the discretization of the flow equations and the evolution equation of the gas fraction are intertwined. This property is fulfilled in Cartesian coordinates, but it has to be adapted to the quasi-two-dimensional case because constant pressure and velocity fields are no more solution of the system (7). In order to derive a stable approximation in case of quasi-two-dimensional flows we propose to consider the fully three-dimensional Saurel-Abgrall scheme on a special mesh that exhibits axisymmetry and also implies rotational symmetry of the discretized equations. In this way we deduce a two-dimensional scheme for the quasi-two-dimensional flow problem. The procedure is similar to the one presented in [6]. Here we briefly recall the resulting non-conservative upwind discretization of the evolution equation for the gas fraction φ.

$$\begin{aligned}
\varphi_{ij}^{n+1} = \varphi_{ij}^{n} \quad - \quad & \frac{\Delta t}{\|V_{ij}\|}\Big(\|\Gamma_{z,i,j+\frac{1}{2}}\|\overline{v}^{\,n}_{z,i,j+\frac{1}{2}}(\overline{\varphi}^{\,n}_{i,j+\frac{1}{2}} - \varphi_{ij}^{n}) - \\
& \qquad \|\Gamma_{z,i,j-\frac{1}{2}}\|\overline{v}^{\,n}_{z,i,j-\frac{1}{2}}(\overline{\varphi}^{\,n}_{i,j-\frac{1}{2}} - \varphi_{ij}^{n})\Big) \\
- \quad & \frac{\Delta t}{\|V_{ij}\|}\Big(\|\Gamma_{r,i+\frac{1}{2},j}\|\overline{v}^{\,n}_{r,i+\frac{1}{2},j}(\overline{\varphi}^{\,n}_{i+\frac{1}{2},j} - \varphi_{ij}^{n}) - \\
& \qquad \|\Gamma_{r,i-\frac{1}{2},j}\|\overline{v}^{\,n}_{r,i-\frac{1}{2},j}(\overline{\varphi}^{\,n}_{i-\frac{1}{2},j} - \varphi_{ij}^{n})\Big),
\end{aligned} \tag{27}$$

where $\overline{\varphi}$, $\overline{v}_z$ and $\overline{v}_r$ denote the gas fraction and the velocity components given by the solution of the Riemann problem at the interfaces $\Gamma_{r,i\pm\frac{1}{2},j}$ and $\Gamma_{z,i,j\pm\frac{1}{2}}$, respectively.

3.3 Fluid-Structure Coupling

For the approximation of the transient two-phase flow problem (7) and the transient elastic solid model (19) Godunov type finite volume schemes are used. From the mathematical as well physical point of view the two systems of equations are coupled at the fluid-structure interface by the transition conditions (22). In the literature

there are different coupling strategies discussed concerning their embedding into numerical methods. These differ in the discretization of the transition conditions and their incorporation into the simultaneous or alternating application of the two solvers. In case of strong coupling the approximations of both the fluid and the structure are updated simultaneously within one time step by a monolithic solver including the complete transition conditions (22) without any splitting technique, see [30]. Opposite to this, the basic idea of weak coupling strategies, also known as partitioned approach or Gauss-Seidel method, see [30], consists of the alternating application of two separate solvers for the fluid and for the solid, respectively, where each solver uses boundary values provided by the other solver. This procedure is now to be detailed.

Let Ω and $\overline{\Omega}$ denote the fluid domain and the solid domain, respectively, that are separated by the fluid-solid interface $\overline{\Gamma}$. In each of these domains we apply the finite volume discretization (23) either for the inviscid flow problem or for the solid mechanical problem, respectively. These can be written in compact form

$$\mathbf{U}^{n+1} = \mathbf{U}^n + \Delta\, t\mathbf{R}_f\left(\mathbf{U}^n\right), \qquad \overline{\mathbf{U}}^{n+1} = \overline{\mathbf{U}}^n + \Delta t\mathbf{R}_s\left(\overline{\mathbf{U}}^n\right), \tag{28}$$

where at the boundaries $\partial\Omega$ and $\partial\overline{\Omega}$ numerical fluxes are computed incorporating the boundary conditions. Except for the fluid-solid interface $\overline{\Gamma} = \partial\Omega \cap \partial\overline{\Omega}$ these are computed by solving a Riemann problem where the exterior state is either given by the boundary conditions or extrapolated from the interior of the domain. At the interface $\overline{\Gamma}$ we have to proceed differently, because from a mathematical and physical point of view the transition conditions (22) have to be fulfilled there for *both* time levels n and $n+1$, i.e.,

$$\mathbf{v}^T(\mathbf{U}^n)\mathbf{n}_{\overline{\Gamma}} = \overline{\mathbf{v}}^T(\overline{\mathbf{U}}^n)\,\mathbf{n}_{\overline{\Gamma}}, \quad \mathbf{n}_{\overline{\Gamma}}^T\,\overline{\boldsymbol{\sigma}}(\overline{\mathbf{U}}^n)\,\mathbf{n}_{\overline{\Gamma}} = -p(\mathbf{U}^n) \quad \text{on} \quad \overline{\Gamma}, \tag{29}$$

$$\mathbf{v}^T(\mathbf{U}^{n+1})\mathbf{n}_{\overline{\Gamma}} = \overline{\mathbf{v}}^T(\overline{\mathbf{U}}^{n+1})\,\mathbf{n}_{\overline{\Gamma}}, \quad \mathbf{n}_{\overline{\Gamma}}^T\,\overline{\boldsymbol{\sigma}}(\overline{\mathbf{U}}^{n+1})\,\mathbf{n}_{\overline{\Gamma}} = -p(\mathbf{U}^{n+1}) \quad \text{on} \quad \overline{\Gamma}. \tag{30}$$

For this purpose the two discretizations (28) are separated into two approximations for the solution of two transient initial boundary value problems corresponding to different systems of equations — one for each solver — , where the transition conditions (22) are split into two boundary conditions for the flow problem and the structure problem, respectively. A naive approach would be the *explicit coupling*, where for the flow solver we prescribe the normal velocity at time level n along the interface, i.e.,

$$\mathbf{U}^{n+1} = \mathbf{U}^n + \Delta t\mathbf{R}_f\left(\mathbf{U}^n\right) \qquad \text{with} \qquad \mathbf{v}^T\mathbf{n}_{\overline{\Gamma}} = \overline{\mathbf{v}}^T(\overline{\mathbf{U}}^n)\mathbf{n}_{\overline{\Gamma}} \quad \text{on} \quad \overline{\Gamma} \tag{31}$$

and the pressure distribution of the fluid along the contact line at time level n provides boundary values for the normal stress of the structure mechanical problem, i.e.,

$$\overline{\mathbf{U}}^{n+1} = \overline{\mathbf{U}}^n + \Delta t\mathbf{R}_s\left(\overline{\mathbf{U}}^n\right) \qquad \text{with} \qquad \mathbf{n}_{\overline{\Gamma}}^T\,\overline{\boldsymbol{\sigma}}\,\mathbf{n}_{\overline{\Gamma}} = -p(\mathbf{U}^n) \quad \text{on} \quad \overline{\Gamma}. \tag{32}$$

Note that the splitting of the transition conditions (22) along the interface can be regarded as an operator splitting.

In (31) and (32) the numerical fluxes at the interface $\overline{\Gamma}$ are computed evaluating the fluxes (8) and (20) in normal direction $\mathbf{n}_{\overline{\Gamma}}$, i.e., $\mathbf{F}_{\overline{\Gamma}} = (\mathbf{F}_z, \mathbf{F}_r)\mathbf{n}_{\overline{\Gamma}}$ and $\overline{\mathbf{F}}_{\overline{\Gamma}} = (\overline{\mathbf{F}}_z, \overline{\mathbf{F}}_r)\mathbf{n}_{\overline{\Gamma}}$, where for the fluid the normal fluid velocity is determined by the normal solid velocity and for the solid the normal stress component is determined by the fluid pressure. All other missing data are taken from the adjacent approximations of the flow problem or the solid problem, respectively, in the interior of the according domain. In particular, in our computations presented in Section 4 we always have $\mathbf{n}_{\overline{\Gamma}} = (1,0)^T$. Then $\mathbf{F}_{\overline{\Gamma}} = \mathbf{F}_z$ with $v_z = \overline{v}_z$ and ρ, p, v_r are the density, pressure and radial velocity taken from the interior of the fluid. Similarly, we compute $\overline{\mathbf{F}}_{\overline{\Gamma}} = \overline{\mathbf{F}}_z$ with $\overline{\boldsymbol{\sigma}}_{zz} = -p$ and $\overline{\boldsymbol{\sigma}}_{zr}$, $\overline{v}_z$, $\overline{v}_r$ are taken from the interior of the solid.

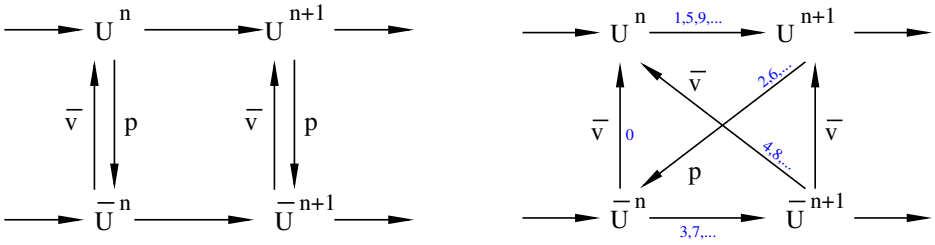

Figure 1: Illustration of explicit coupling (left) and implicit coupling (right).

Since in (31) and (32) we exchange both pressure p and normal velocity $\overline{\mathbf{v}}^T\mathbf{n}_{\overline{\Gamma}}$ at time level n, see Figure 1 (left), the transition conditions (22) are not satisfied at the new time level $n+1$, i.e., (30) does not hold, resulting in a kinetic and a dynamic approximation error ϵ_k and ϵ_d, respectively, at the interface $\overline{\Gamma}$

$$\epsilon_k := \mathbf{v}^T(\mathbf{U}^{n+1})\mathbf{n}_{\overline{\Gamma}} - \overline{\mathbf{v}}^T(\overline{\mathbf{U}}^{n+1})\,\mathbf{n}_{\overline{\Gamma}} \neq 0, \quad \epsilon_d := \mathbf{n}_{\overline{\Gamma}}^T\,\overline{\boldsymbol{\sigma}}(\overline{\mathbf{U}}^{n+1})\,\mathbf{n}_{\overline{\Gamma}} + p(\mathbf{U}^{n+1}) \neq 0. \quad (33)$$

Therefore the explicit coupling approach will fail. Instead we prefer an *implicit coupling* where we *alternately* exchange values for the pressure p and the normal velocity $\overline{\mathbf{v}}^T\mathbf{n}_{\overline{\Gamma}}$ at the contact line. Starting with the fluid problem the implicitly coupled problem reads:

$$\mathbf{U}^{n+1,k+1} = \mathbf{U}^n + \Delta t\mathbf{R}_f\left(\mathbf{U}^{n+1,k}\right) \text{ with } \mathbf{v}^T\mathbf{n}_{\overline{\Gamma}} = \overline{\mathbf{v}}^T(\overline{\mathbf{U}}^{n+1,k})\mathbf{n}_{\overline{\Gamma}} \text{ on } \overline{\Gamma}, \quad (34)$$

$$\overline{\mathbf{U}}^{n+1,k+1} = \overline{\mathbf{U}}^n + \Delta t\mathbf{R}_s\left(\overline{\mathbf{U}}^{n+1,k}\right) \text{ with } \mathbf{n}_{\overline{\Gamma}}^T\,\overline{\boldsymbol{\sigma}}\,\mathbf{n}_{\overline{\Gamma}} = -p\left(\mathbf{U}^{n+1,k+1}\right) \text{ on } \overline{\Gamma}. \quad (35)$$

Alternatively, one may start with the solid problem. The system (34) and (35) can be regarded as a fixed point iteration initialized with $\mathbf{U}^{n+1,0} = \mathbf{U}^n$ and $\overline{\mathbf{U}}^{n+1,0} = \overline{\mathbf{U}}^n$. In the literature the repetition of this procedure for $k = 0, 1, \ldots$, until convergence is referred to as *strong coupling*, see [31, 45]. It is illustrated in Fig. 1 (right). In case of convergence, the fixed point $\mathbf{U}^{n+1} = \lim_{k\to\infty}\mathbf{U}^{n+1,k}$ and $\overline{\mathbf{U}}^{n+1} = \lim_{k\to\infty}\overline{\mathbf{U}}^{n+1,k}$ satisfies the transition conditions (22), i.e., (30) holds. Due to the explicit time stepping the numerical fluxes have to be computed only once in the *entire* domain. Then one fixed point iteration only requires to update the numerical fluxes near to the fluid-solid interface and the data in the cells attached to the interface. This

makes the fixed point iteration costly. Therefore we prefer to use a so-called *weak coupling*, see [31, 45], where we perform only *one* iteration step. Herein the values for the pressure and the normal velocity at the fluid-solid interface are exchanged alternately in time. Starting again with the fluid problem the coupled problem then reads

$$\mathbf{U}^{n+1} = \mathbf{U}^n + \Delta t \mathbf{R}_f\left(\mathbf{U}^n\right) \text{ with } \mathbf{v}^T \mathbf{n}_{\overline{\Gamma}} = \hat{\kappa}_f^n \, \overline{\mathbf{v}}^T(\overline{\mathbf{U}}^n)\mathbf{n}_{\overline{\Gamma}} \quad \text{on } \overline{\Gamma}, \tag{36}$$

$$\overline{\mathbf{U}}^{n+1} = \overline{\mathbf{U}}^n + \Delta t \mathbf{R}_s\left(\overline{\mathbf{U}}^n\right) \text{ with } \mathbf{n}_{\overline{\Gamma}}^T \, \overline{\boldsymbol{\sigma}} \, \mathbf{n}_{\overline{\Gamma}} = -\hat{\kappa}_s^n \, p\left(\mathbf{U}^{n+1}\right) \text{ on } \overline{\Gamma}. \tag{37}$$

Obviously, the transition conditions (22) are not satisfied at the new time level $n+1$, i.e., (30) does not hold. The error is in the order of the time step size that is small for explicit time discretizations. However, due to the alternating time integration of the schemes, this error is accumulating with increasing number of time steps. In order to damp the accumulated error we introduce in (36), (37) the parameters $\hat{\kappa}_f^n$ and $\hat{\kappa}_s^n$. Choosing $\hat{\kappa}_f^n = \hat{\kappa}_s^n = 1$, then (36), (37) coincides with the first iteration step of the strong coupling (34), (35). In Section 3.3.2 we will discuss how to choose these parameters.

The time evolution between levels n and $n+1$ of the weak coupling procedure (36), (37) consists of the four following logical steps after having initialized the data in the fluid and solid domain.

1. The velocity on time level n as well as the coordinates of the solid grid vertices along the fluid-solid interface $\overline{\Gamma}$ are transferred from the structure solver to the flow solver.

2. The flow solver executes the computation for one time step according to (36) using a previously determined time step size Δt as well as deformation velocities in normal direction $\overline{\mathbf{v}}^T\left(\overline{\mathbf{U}}^n\right)\mathbf{n}_{\overline{\Gamma}}$ along the fluid-structure interface $\overline{\Gamma}$ provided by the solid solver as boundary conditions for the two-phase flow problem.

3. The pressure on the new time level $n+1$ as well as the coordinates of the flow grid vertices along the fluid-solid interface $\overline{\Gamma}$ that may change due to local grid adaptation are copied first from the flow solver to the solid solver.

4. The solid solver updates the stresses and deformation velocities inside the solid domain $\overline{\Omega}$ according to (37) using a previously determined time step size Δt as well as the pressure values $p\left(\mathbf{U}^{n+1}\right)$ along the fluid-structure interface $\overline{\Gamma}$ provided by the flow solver as boundary conditions.

This coupling procedure including the initialization step is sketched in Fig. 2. So far the coupling of both codes has been realized, where both methods use the same time step size, i.e., $\Delta\, t = \overline{\Delta\, t}$. The choice of the time step is discussed later on in Section 3.3.2

3.3.1 Implementation of weak coupling strategy

The two finite volume schemes approximating the fluid and the solid equations, respectively, are realized by two different solvers, where each solver has access only

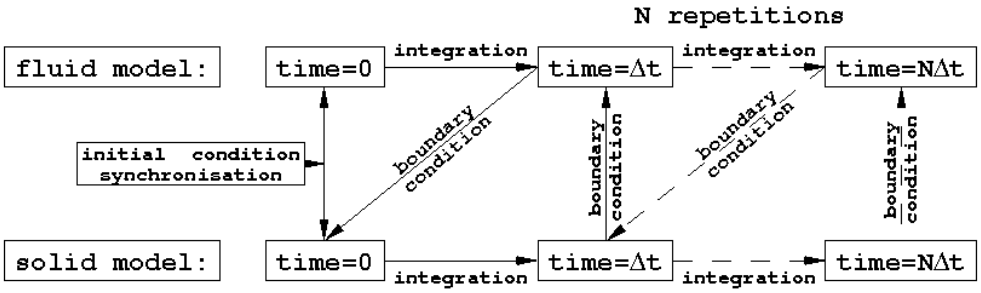

Figure 2: Weak coupling.

to its own exactly defined segment of the computer main memory. For the data exchange between the solvers we use the shared memory and semaphores libraries [44] that offers the opportunity to allocate so-called shared memory segments located in the main memory which can be used via library functions by several C- or C++-codes simultaneously. This open source library uses functions of the linux operation system for the process control and the memory management. The great achievement of the shared memory library can be seen in a logical abstraction of sophisticated management activities of the operation system using a programming interface of objects for the shared memory segments with class functions for the data transfer and access permission control. Sending and receiving semaphoric signals to allow and forbid the access to the shared memory segments provides also possibilities to synchronize both processes similar to strategies for parallel computing and to avoid data access conflicts. Our implementation is based on four shared memory segments:

- Two segments transfer the boundary data together with geometrical informations such as the position of the boundary grid vertices or the normal vectors composed as long data structures; one segment is needed for each direction of data exchange to prohibit conflicts within the communication procedures. A write statement for a data update in one of these segments is followed by setting an allowing semaphore for accesses by the other program. In the other direction a semaphore for waiting has to protect a read access to prohibit a data update on the same shared memory segment at the same time.

- Another pair of shared memory segments is needed for the exchange of informations concerning time step sizes, the number of grid points along the coupling boundary as well as the structure of the data records transferred by the other two shared memory segments. Again one shared memory segment is used for each direction of communication. Observe that the adaptation possibility of our numerical scheme in general leads to changes of the number of grid vertices and cells during the simulation resulting in changes of the structure of the transferred data records. Thus this other pair of shared memory segments is needed to inform in advance how many data have to be received.

The data transfer via shared memory is complicated by many facts. For instance, the copy function of the operation system used by the library only works with static

arrays of fixed length. However, grid adaptation at the coupling boundary can be implemented in an appropriate manner using dynamic data structures. Furthermore the use of semaphores can cause a kind of delay phenomena between writing and reading statements. Therefore identity numbers at the begin and at the end of the data records are used as a kind of stamp to ensure that all sent data characterized in this way are received by the other program, which checks these identifications and the correct ordering within the communication processes.

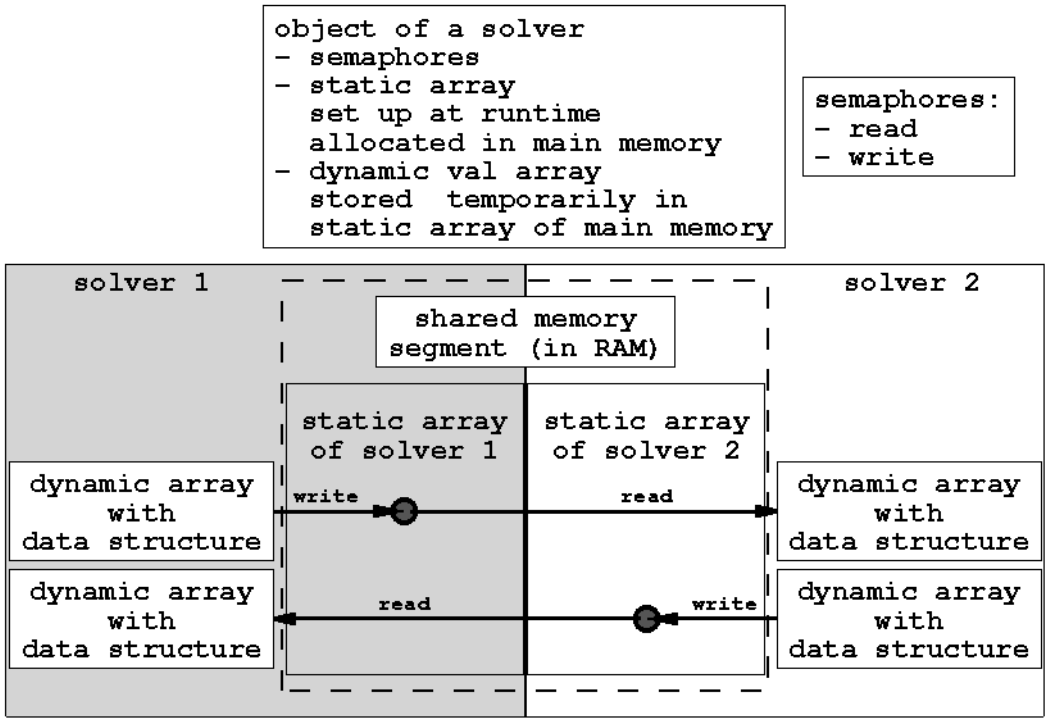

Figure 3: Shared memory segments.

In the following we will give an example for the realization of data exchanges between two processes using functions of the shared memory library as well as different data structures as illustrated in Fig. 3:

1. *Initialization of shared memory segments.* Two shared memory segments for time and data block structure informations and two segments for field data along the coupling boundary are allocated within each program and according objects are created using a library function by one of the two processes depending on the direction of the data transfer. Estimates for the size of the allocated segments are based on the size of the coarsest grid for both solvers as well as the chosen maximal number of refinement levels.
   The same library function creates also objects for the previously allocated segments for its access if the coupled process calls this function without size specification. So altogether each program can access to two pairs of shared memory segments. These four shared memory segments are available within

both C++-codes by four objects equipped with class functions to write the content of a static array to the corresponding shared memory segment, to copy from this shared memory segment into a static array and to set semaphores to control the access permissions to the managed shared memory segment.

2. *Determine data size information.* Each solver determines the grid vertices along the fluid-solid interface as well as the resulting structure of the records for the data transfer along the interface. In particular, the size and the uniform distance of an intermediate grid for the data transfer are calculated from the minimal distance of grid nodes on the coupling boundary.

3. *Send transfer information.* The first index of each of the different blocks within the data records as well as the initial time zero and a control number to identify the data set are written to the shared memory segment using a static array. By this data exchange the other process is informed about the structure of the data records to be received; the thereby received control number is also used to identify records within the transfer of the boundary data. A read access to the updated contents of the shared memory segment is allowed by setting the according semaphore by the object class function. For each direction of the communication between the two programs an own shared memory segment for data structures is used to circumvent communication conflicts.

4. *Interpolation.* Each solver interpolates the data read from the computational, locally refined grid along the fluid-solid interface onto an equidistant intermediate grid of the previously determined size. Then each of them composes the data records containing blocks for solid stress components or fluid pressure, respectively, normal velocities and normal directions and control numbers to identify the data record within the communication.

5. *Data sending.* The write class function of the shared memory segment object for the field data along the interface transfers the previously composed data record to this shared memory segment. Again each process uses another segment for this data exchange to avoid communication conflicts.

6. *Data receiving.* Using the read class function of the shared memory segment object the data record of the coupled program is copied from the according shared memory segment into an array of the own program. The reading procedure is repeated until a data record with the expected control number is found. The control number is known as a result of the data exchange procedure concerning data structure informations using the other pair of shared memory segments. Then the received data record is split into the different data blocks and their contents is stored in dynamic fields of the program for a later evaluation of boundary conditions.

7. *Preparing data transfer for next time step.* Each process increments its control number to identify the data sets for the next data transfer.

We conclude this section with two remarks on spatial and temporal interpolation at the coupling boundary.

Remark 1: *(Spatial interpolation).* Properties of the spatial interpolation for the exchange of field variables are often discussed in the context of coupling methods using non-matching grids at the interface. In particular, conservation properties or variational principles of continuum mechanics are of interest. Our investigations using different interpolation strategies show only small differences in case of high grid resolution. This also holds true for discretizations with hanging nodes due to local grid refinement, if the adaptation process is conservative. The results presented in Section 4 are obtained using the highest possible resolution along the whole coupling boundary. In this case the intermediate grid coincides with at least one computational grid of the two solvers along the interface.

Remark 2: *(Temporal interpolation).* To overcome the assumption of identical time step sizes for the coupled solvers an additional interpolation with respect to the time variable is needed. Such an interpolation of the boundary values of one solver onto the time level of the coupled method ensures the mathematical and physical accuracy of the transient coupling. However, it also induces a further approximation error. On the other hand, the higher flexibility concerning the choices of the time step sizes for both schemes can be used to reduce the approximation errors within other parts of the computational domain of each medium. We want to investigate this in the future.

3.3.2 Error reduction of weak coupling

Due to the weak coupling (36) and (37) the transition conditions (22) are in general not fulfilled at the new time level $n+1$, see (33), no matter how we choose the parameters $\hat{\kappa}_f^n$ and $\hat{\kappa}_s^n$. In particular, for $\hat{\kappa}_f^n = \hat{\kappa}_s^n = 1$, i.e., the weak coupling (36), (37) coincides with the first iteration step of the strong coupling (34), (35), an accumulation of the error with increasing number of time steps can be observed in computations. In order to reduce the error in the transition conditions, see (33), we introduced in (36), (37) the damping factors $\hat{\kappa}_f^n$ and $\hat{\kappa}_s^n$ for the fluid and the solid, respectively, as additional degree of freedom. The idea is to choose the parameters $\hat{\kappa}_f^n$ and $\hat{\kappa}_s^n$ such that the error (33) is locally reduced and the maximal possible CFL number for a stable integration is attained within the following time integration step. This procedure is similar to Lagrange multipliers within formulations of mechanical principles, for instance that of virtual work in [30].

First of all, we notice that so-called von Schmidt waves develop in the liquid near the fluid-solid interface due to different wave propagation velocities within the materials. This phenomena will be explained later on in Section 4 in more detail. Therefore the criterion for the linear stability has to take into account the eigenvalues of both coupled systems of equations to ensure a stable numerical approximation of such interface wave phenomena. Otherwise not all possible waves lying in the region of dependence would be captured by the scheme. Hence, the time step size $\Delta t = \overline{\Delta t}$ has to fulfill the following two CFL conditions

$$\frac{\Delta t}{\|V\|} \leq \frac{\nu_0}{\lambda_{f,max}}, \quad \frac{\overline{\Delta t}}{\|\overline{V}\|} \leq \frac{\nu_0}{\lambda_{s,max}} \tag{38}$$

with maximal characteristic speeds

$$\lambda_{f,max} = \max\{|\mathbf{v}|, |\mathbf{v} \pm c|\}, \quad \lambda_{s,max} = \max\{|c_1|, |c_2|\} \tag{39}$$

in the fluid and the solid, respectively. Here ν_0 denotes an upper bound for the CFL number for which the linear stability of the discretization is ensured, i.e., $\nu_0 \leq 0.5$ for a standard Godunov type method.

In order to determine the damping parameters $\hat{\kappa}_f^n$ and $\hat{\kappa}_s^n$ we introduce the actual CFL numbers corresponding to a time step t_n for the schemes on the fluid side and the solid side of the fluid-structure interface, respectively,

$$\nu_f^n := \frac{\Delta t\, \lambda_{f,max}^n}{\|V\|}, \quad \nu_s^n := \frac{\overline{\Delta t}\, \lambda_{s,max}^n}{\|\overline{V}\|} \tag{40}$$

and define the ratios of maximal and actual CFL number

$$r_f^n := \frac{\nu_0}{\nu_f^n}, \quad r_s^n := \frac{\nu_0}{\nu_s^n}. \tag{41}$$

By means of these values we introduce the exponential smoothing

$$\kappa_f^n := \left(r_f^n\right)^{q_1 + \frac{2}{\pi}\arctan(r_f)(q_\infty - q_1)}, \quad \kappa_s^n := \left(r_s^n\right)^{q_1 + \frac{2}{\pi}\arctan(r_s)(q_\infty - q_1)} \tag{42}$$

with empirical exponents $q_1 = 0.95$ and $q_\infty = 0.5$. Note that for $q_1 = q_\infty = 1$ we have $\kappa_f^n = r_f^n$ and $\kappa_s^n = r_s^n$, respectively. For damping purposes we finally average the damping parameters over the last two time steps to avoid an oscillating behavior of the damping parameters, i.e.,

$$\hat{\kappa}_f^n := \frac{1}{2}(\kappa_f^n + \kappa_f^{n-1}), \quad \hat{\kappa}_s^n := \frac{1}{2}(\kappa_s^n + \kappa_s^{n-1}). \tag{43}$$

Using these parameters in our computations we observed a significant reduction of the error (33). Evidence for this is given by the numerical results presented in Section 4.

4 Numerical Simulation

For the investigation of the mechanism of cavitation damaging we have simulated numerically the collapse of a single cavitation bubble near the surface of a dynamically reacting, linear elastic solid, see Fig. 4. Here the focus of our interests is on the effects of the dynamical processes within the structure that are initiated by the interaction with the adjacent two-phase flow of a collapsing bubble. In particular, we are going to analyze whether the stress states exceed breaking points of the solid material. This might provide an explanation for cavitation erosion observed in experiments.

Computational setup. The bubble is a sphere with radius $r = 1$ mm separating the gas inside from the surrounding liquid. The distance between the bubble origin and the solid surface is twice the radius of the cavitation sphere, i.e., $d = 2r$.

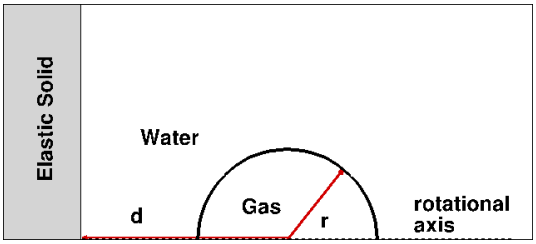

Figure 4: Configuration of a gas-filled bubble in an liquid environment next to an elastic solid.

A high pressure gradient due to the gas pressure of 2118 Pa and the liquid pressure of 5×10^7 Pa causes the collapse of the bubble. The ambient liquid density of 1000 kg/m^3 and the gas density of $\rho_{gas} = 0.0266$ kg/m^3 correspond to a sound speed of about 1480 m/s, and 340 m/s, respectively. For a detailed discussion for this choice of initial data we refer to [50]. For the solid material we choose steel characterized by the density $\overline{\rho} = 7800$ kg/m^3 and Young's modulus $E = 210 \times 10^9$ Pa leading to the velocities $c_1 = 5990$ m/s and $c_2 = 3458$ m/s for the dilatation waves and for the shear waves, respectively. Initially we assume that the forces between the liquid and the adjacent structure are in equilibrium. Therefore we set the stress component orthogonal to the contact line identically to the liquid pressure, i.e., $\overline{\boldsymbol{\sigma}}_{zz} = -p$. All three phases are supposed to be at rest. The computational domain consists of two parts $\overline{\Omega} = [-0.04, 0.01] \times [0, 0.05]$ m^2 and $\Omega = [0.01, 0.06] \times [0, 0.05]$ m^2 for the solid and the fluid, respectively, that are connected at the contact line $\overline{\Gamma} = \{0.01\} \times [0, 0.05]$. These are discretized by 16×16 and 4×4 cells on the coarsest grid, respectively. The use of up to $L = 9$ refinement levels can lead to a resolution of $16 \times 2^L = 8192$ cells in each spatial direction for the solid grid and up to $4 \times 2^L = 2048$ cells concerning the flow discretization. The fluid solver and the solid solver use the same time step size $\Delta t = \overline{\Delta t} = 10^{-10} s$ which fulfills the linear stability criterion for both methods with respect to the finest mesh. The efficiency is significantly improved by grid adaptation that is performed inside the adaptation region determined by a circle with center point in $[0.01, 0.0]$ m and radius 0.01 m, whereas outside we use the coarse discretization corresponding to $L = 0$. To avoid metric jumps at the boundary of the adaptation region the grid is graded near to its boundary.

The computations were performed on the system 8×4 core AMD Opteron 8356, 2.3 GHz, 256 GB Ram. The computational time for the presented simulation of a physical time interval of about 65×10^{-6} seconds was about six weeks. This large time consumption was caused by (i) the high resolution that requires small time steps due to the explicit time stepping and (ii) the fact that we have been using the same time step for both the fluid solver and the solid solver.

Bubble collapse. The collapse of a bubble near to a rigid wall without fluid-structure interaction has been investigated for the present scenario in previous work [51, 4]. We will briefly summarize the dynamical process. Later on we will then discuss in detail additional effects caused by the fluid-structure interaction. Due to the lower pressure inside the bubble a rarefaction wave is emitted into the liquid and

a shock wave runs towards the bubble center. The rarefaction wave is being reflected at the solid surface. The reflected wave moves towards the bubble. At the proximal side of the bubble that is nearest to the wall it is partially reflected into the liquid and partially transmitted into the bubble because of the lower acoustic impedance of the gas. Inside the bubble the transmitted wave interacts with the shock wave that is being reflected in the bubble center, while in the liquid the wave interaction process between the solid and the bubble continues where the wave strength decreases with each interaction. Due to the shock wave the gas inside the bubble is accelerated towards the bubble center, i.e., the bubble starts shrinking. However, due to the wave interactions at the bubble interface, the bubble surface is more accelerated at the distal side, i.e., the part of the bubble farthest from the wall. This results in an indentation of the bubble surface at the distal side. A liquid jet is forming that is directed towards the wall. This water jet penetrates the bubble at the proximal side and hits the wall. The remaining toroidal bubble starts a translational movement towards the wall.

In principle, the wave dynamics is very similar when performing the same computation with an elastic solid instead of a rigid solid. This is true as long as Young's modulus characterizing the elastic material is large enough, e.g. steel. Otherwise there might be a phase change during the reflection at the wall. The development of the bubble shape in case of an elastic wall is presented in Figs. 5, 7, 9, 11 and 13 exhibiting the rarefaction waves and the shock wave in the liquid and the gas, respectively, the shrinking of the bubble, the collapse of the bubble and its penetration by the water jet directed towards the solid and the so-called water-hammer shock emitted into the liquid and finally the elongation of the bubble when moving towards the wall. Here the absolute value of the density gradient at different time steps is plotted using a logarithmic scale. In these figures rarefaction waves and shock waves can be observed that are emitted from the bubble wall into the liquid or into the gas and are reflected at the fluid–solid interface and the bubble interface. When these waves hit the surface of the structure they cause a transient change of load and, hence, stress and deformation waves develop in the structure, see Figs. 6, 8, 10, 12 and 14. Reversely, the waves in the structure interact with the two-phase flow via the boundary condition for the flow velocity in normal direction causing von Schmidt waves in the fluid. In the following we will address in detail the additional phenomena resulting from the fluid-structure interaction.

von Schmidt waves. For most solid materials used within technical applications the propagation speed for dilatation waves as the fastest phenomena inside the structure is significantly larger than the sound-propagation velocity of the adjacent liquid. For instance, the speed of the dilatation waves for steel are about 6000 m/s whereas shock and rarefaction waves in water at rest propagate with about 1500 m/s at room conditions. This difference in the wave speeds at both sides of the fluid-solid interface causes so-called von Schmidt waves that can be observed in Fig. 5: compression or rarefaction waves emitted from the bubble propagate in the liquid with the corresponding speed of sound toward the liquid-structure interface. When such a wave front hits the surface of the solid, the coupling algorithm transfers the wave by changes of the normal stress component into the solid leading to stress waves inside the solid. Depending on the direction of molecular motion the initiated phenomena

propagates either with the speed for the shear waves or that for the dilatation waves, respectively, which are both larger than the sound speed in the adjacent liquid. The stress waves in the solid are always accomplished by changes of the deformation velocity which arise within the reverse coupling as a boundary condition for the liquid along the fluid-structure interface. These changes of the boundary values for the velocity in normal direction with respect to the coupling boundary initiates a new wave within the liquid – the von Schmidt wave. At the interface the transversal wave in the solid causes also motions of the molecules parallel to the wave front, i.e., orthogonal to the coupling boundary, because of the higher number of the degrees of freedom at the boundary. These motions normal to the interface are transferred to the flow via the kinematic transition condition moving faster than the sound speed in the liquid. This causes a von Schmidt wave in the liquid that looks similar to a Mach cone and a triangle in three and two space dimensions, respectively, as a consequence of the supersonic perturbation of the fluid flow. This von Schmidt wave can be seen in Fig. 5. It is a special wave phenomena caused by the interaction of two dynamical systems, see [46].

On the structure side of the interface the slower propagation of the pressure loads in comparison with the stress waves causes a circulation of the displacement velocities as illustrated in Fig. 6. There another von Schmidt wave develops in the structure that connects the motions in transversal direction induced by the dilatation waves with the slower shear wave.

When the computation proceeds these two phenomena of von Schmidt waves in the liquid and the circular orientation of the structure displacements near the coupling boundary characterize every change of loadings at the solid surface as consequences of bubble wall motions. Hence, Fig. 7 shows a system of interacting wave fronts and von Schmidt waves in the fluid whereas the diameters of the eddies for the displacements become larger in the solid when the stress wave fronts move away from the axis of symmetry as presented in Fig. 8.

In order to verify the adherence of the kinematic transition condition we plot the velocity component normal to the interface in the fluid and the solid, see Fig. 15. Analogously the continuity of the normal forces across the coupling boundary can be investigated. For this purpose we present in Fig. 16 fluid pressure as well as the normal stress component $\overline{\boldsymbol{\sigma}}_{zz}$ of the structure.

Material damage. Since the linear elastic model, see Section 2.2, does not account for plastic deformation, we cannot directly conclude from our computations on material damage. However, by a post-processing analysis we can analyze whether the pure elastic range of the solid material has been exceeded during the computation. This may be considered as an explanation of cavitation damaging. For this purpose the comparison of the solid stress states with the von Mises stress is typically used as a criterion for isotropically modeled and work hardening materials as metal or steel. This criterion is based on the hypothesis that the material yields irreversible and breaks if the yield stress exceeds certain tolerances, see [46]. Regarding the general case of a solid stress state in three space dimensions the so-called von Mises comparison stress $\overline{\boldsymbol{\sigma}}_{vM} := \sqrt{3\, I_2}$, see [36, 41], is proportional to the square root of the second invariant $I_2 = \frac{1}{2}\overline{\boldsymbol{\sigma}}^d : \overline{\boldsymbol{\sigma}}^d$ of the stress deviator $\overline{\boldsymbol{\sigma}}^d := \overline{\boldsymbol{\sigma}} - \frac{1}{3} tr\,(\overline{\boldsymbol{\sigma}})\,\mathbf{I}$.

In terms of cylindrical coordinates the von Mises comparison stress reads, see [42],

$$\overline{\boldsymbol{\sigma}}_{vM} = \sqrt{\frac{1}{2}\left(\left(\overline{\boldsymbol{\sigma}}_{zz} - \overline{\boldsymbol{\sigma}}_{rr}\right)^2 + \left(\overline{\boldsymbol{\sigma}}_{zz} - \overline{\boldsymbol{\sigma}}_{\phi\phi}\right)^2 + \left(\overline{\boldsymbol{\sigma}}_{rr} - \overline{\boldsymbol{\sigma}}_{\phi\phi}\right)^2\right) + 3\overline{\boldsymbol{\sigma}}_{zr}^2}. \tag{44}$$

The von Mises comparison stress is used within the yield criterion. One of the most frequently applied approaches for a yield criterion used in the context of the materials considered here, see [36, 41, 42], is based on the difference between the von Mises comparison stress and the yield stress $Y(\lambda)$:

$$\Phi(\overline{\boldsymbol{\sigma}}, \lambda) := \overline{\boldsymbol{\sigma}}_{vM} - Y(\lambda). \tag{45}$$

Herein $\lambda \geq 0$ denotes the plastic multiplier indicating whether the stress state lies within the pure elastic region of the stress-strain relation, i.e., $\lambda = 0$, or a plastic part has to be taken into account by $\lambda := \frac{\mu}{\mu_p} - 1 > 0$ using the plastic modulus μ_p, see [46]. By the yield criterion (45) elastic and plastic deformation can be distinguished by $\Phi(\overline{\boldsymbol{\sigma}}, \lambda) < 0$ and $\Phi(\overline{\boldsymbol{\sigma}}, \lambda) \geq 0$, respectively.
For λ an additional transport equation can be derived leading to a significant computational effort for the application of this yield criterion. To avoid the numerical approximation of this partial differential equation and, hence, to get only an estimate for the yield boundary of the structure we use the yield strength Y_0 as constant approximation for the yield criterion neglecting the effect of strain hardening, i.e.,

$$Y(\lambda) = Y_0. \tag{46}$$

In [65] a much simpler yield criterion based on the same ansatz is used. The advantage of such simplifications is that the criterion can be directly evaluated based on the calculated values for the stress components in a post-processing step without solving an additional differential equation. On the other hand this criterion does not allow to describe the transient development of plastic zones by the correct propagation speeds but only the spatial directions of their expansion.

The yield strength Y_0 depends on the specifications and the state of the steel. To get an idea whether steel could be deformed plastically due to the waves emitted in the bubble collapse the post-processing analysis was executed twice using two values for the yield strength following [71], one for structural steel ($Y_0 = 250\,\mathrm{MPa}$) and one for stainless steel ($Y_0 = 502\,\mathrm{MPa}$). In Figs. 17 to 20 we present the results of the evaluation of the function $\Phi(\overline{\boldsymbol{\sigma}}) = \overline{\boldsymbol{\sigma}}_{vM} - Y_0$ as simplified yield criterion in the time range $50.0\,\mu s$ to $56.0\,\mu s$ for structural steel (left) and stainless steel (right). The results show a zone of plastic deformation at the symmetry axis caused by the impact of the water-hammer shock wave on the solid surface. The initiated stress waves transport the plastic zone in the direction of both cylindrical coordinates r and z. The increase of its area is accomplished by a decrease of its intensity, i.e., the von Mises yield criterion reaches again the elastic region. Altogether an almost spherical region with center point close to the corner of the symmetry boundary and near to the coupling boundary exists where the states exceed the yield criterion indicating that plastic deformation might occur there. There material damage in the sense of plastic deformation might be expected.

Note that the von Mises comparison stress $\overline{\boldsymbol{\sigma}}_{vM}$ exceeds the yield strength Y_0 only if the value characterizing structural steel is applied but not for stainless steel. Using yield strength values of aluminum or copper the yield criterion $\Phi(\overline{\boldsymbol{\sigma}})$ then exhibits large plastic zones within the solid domain that can be observed in Fig. 21 for a long time interval of the simulation. Note, however, that these evaluations are not consistent with the simulations because the density and the wave speeds of steel were used by the solid solver. Nevertheless the results indicate that materials with lower yield strength values are probably damaged essentially by the waves emitted by the adjacent collapsing cavitation bubble. Simulations using different parameter settings for the solid density, the speeds of dilatation and shear waves as well as the yield strength characterizing several materials should improve this kind of investigations in the future.

Finally we want to emphasize that fundamental assumptions of the applied structure mechanical model, see Section 2.2, are no longer valid if yield bounds of the solid material are reached or exceeded. The presented investigations are concerned with the question whether the plastic region of the stress-strain relation of the solid material could be reached within the model problem. A realistic description of plastic effects, transient yield bounds, deforming computational regions and their interactions with the flow problem needs extensive improvements of the material model and the numerical algorithms.

5 Conclusion

As a model problem to investigate cavitation damaging the collapse of a single gas bubble collapsing near to an elastic solid wall is simulated numerically. The transient three-phase system is modeled by the compressible Euler equations completed by a stiffened gas law for both fluids, where the liquid and the gas phase are distinguished by the gas fraction and the elastodynamical equations for a linear-elastic solid. The two systems of equations for the fluids and for the solid are coupled by transition conditions at the fluid-solid interface.

The balance laws for fluid and solid are discretized by adaptive finite volume schemes, whereas for the evolution of the gas fraction a non-conservative upwind discretization originally developed by Saurel and Abgrall is applied. The latter prevents pressure and velocity oscillations at the liquid-gas interface.

A weak coupling strategy connects the alternating calculations of the fluid solver and the solid solver using transient boundary conditions that are updated by the other solver. The inter-solver communication is realized by a library for shared memory segments within the main memory of the computer accessible by both codes. Between the two solvers library functions for write and read access of data structures as well as for control of semaphores allow to exchange boundary values of the approximations obtained by the two methods via intermediate grid and spatial interpolation along the coupling boundary. Stability aspects as well as the implementation of the code coupling were regarded.

First numerical results show significant effects of the dynamical processes inside the solid on the bubble collapse and the wave phenomena in the fluid. Shock waves

emitted from the collapsing bubble cause stress waves inside the structure which exceed the yield strength of structural steel within an almost spherically shaped region with its center on the symmetry axis at the solid surface. Such phenomena might be an explanation for cavitation damaging. Further investigations using several parameter settings for different solid materials are intended to identify situations where the plastic region of the stress-strain relation is reached. A realistic description of plastic effects needs extensive improvements concerning the structure modeling as well as the numerical method.

So far the coupling procedure is realized under the very restricting assumptions that both solvers use the same time step size and the size of an intermediate grid for the data transfers has to take into account the discretizations of both coupled methods. In the future we want to relax these assumptions.

Due to severe numerical dissipation inherent in the stiffened gas approach, the liquid-gas interface is significantly smeared and a numerical phase transition zone can be observed in the computations, cf. [50, 51]. Here the ghost fluid method turned out to give much better results at the same resolution level for the problem of a laser-induced collapsing bubble. We therefore will replace the Saurel-Abgrall approach by the ghost fluid method, cf. [68, 24], that has already been implemented and validated by numerous computations presented in [4].

6 Bibliography

[1] Abgrall R., (1996), "How to prevent pressure oscillations in multicomponent flow calculations: A quasi-conservative approach", J. Comput. Phys., **125**, 150-160.

[2] Abgrall R., Karni S., (2001), "Computations of compressible multifluids", J. Comp. Phys., **169**, No.2, 594–623.

[3] Abgrall R., Karni S., (2001), "Ghost-fluids for the poor: A single fluid algorithm for multifluids", in Hyperbolic Problems: Theory, Numerics, Applications, H. Freistühler, G. Warnecke (eds.), Birkhäuser Verlag, 1–10.

[4] Bachmann M., (2012), "Dynamics of Cavitation Bubbles in Compressible Two-Phase Fluid Flow using Adaptive Parallel Multiscale Schemes", PhD thesis, RWTH Aachen, to be published online.

[5] Bachmann M., Helluy Ph., Jung J., Mathis H., Müller S., (2009), "Random sampling remap for compressible two-phase flows", Research Report, Institut de Recherche Mathématique Avancée de Strasbourg, `http://hal.archives-ouvertes.fr/docs/00/54/69/19/PDF/lagproj.pdf`.

[6] Barberon T., Helluy Ph., Rouy S., (2003), "Practical computation of axisymmetrical multifluid flows", International Journal of Finite Volumes, **1**, No. 1, 1–34.

[7] Behruzi P., Dickopp Ch., Ballmann J., (1999), "Influence of a Thin-Walled Plate on the Collapse of a Cavitation Bubble", in Proceedings of ECCM 99, Munich, Germany, August 31-September 3, 1999, published on CD-Rom.

[8] Benjamin T.B., Ellis A.T., (1966), "The collapse of cavitation bubbles and the pressure thereby produced against solid walls", Phil. Trans. R. Soc. Lond. A, **260**, 221–240.

[9] Best J.P., (1993), "The formation of toroidal bubbles bubbles upon the collapse of transient cavities", J. Fluid Mech., **251**, 79–107.

[10] Blake J.-R., Gibson D.C., (1987), "Cavitation bubbles near boundaries", Ann. Rev. Fluid. Mech., **19**, 99–123.

[11] Blake J.-R., Taib B.B., Doherty G., (1987), "Transient cavities near boundaries", J. Fluid. Mech., **181**, 197–212.

[12] Brackbill J.U., Kothe D.B., Zemach C., (1992), "A continuum method for modeling surface tension", J. Comp. Phys., **100**, 335–354.

[13] Brujan E.-A., Nahen K., Schmidt P., Vogel A., (2001), "Dynamics of laser–induced cavitation bubbles near an elastic boundary", J. Fluid. Mech., **433**, 251–281.

[14] Brujan E.-A., Nahen K., Schmidt P., Vogel A., (2001), "Dynamics of laser–induced cavitation bubbles near elastic boundaries: influence of the elastic modulus", J. Fluid. Mech., **433**, 283–314.

[15] Chern I.-L., Glimm J., McBryan O., Plohr B., Yaniv S., (1986), "Front tracking for gas dynamics", J. Comp. Phys., **62**, 83–110.

[16] Cocchi J.-P., Saurel R., (1997), "A Riemann problem based method for the resolution of compressible multimaterial flows", J. Comput. Phys., **137**, No. 2, 265–298.

[17] Colella Ph., Glaz HM., (1985), "Efficient Solution Algorithms for the Riemann Problem for Real Gases", J. Comput. Phys., **59**, 264–289.

[18] Dickopp Ch., (1996), "Ein Navier-Stokes Löser zur Simulation kollabierender Kavitationsblasen in der Nähe elastischer Festkörperoberflächen", PhD thesis, RWTH Aachen, Shaker-Verlag.

[19] Dickopp Ch., Ballmann J., (1996), "Wave processes in a three phase system of a collapsing bubble near a compliant wall", in Hyperbolic Problems: Theory, Numerics, Applications, J. Glimm et al. (eds.), Singapore: World Scientific, 307–312.

[20] Dickopp Ch., Ballmann J., (1998), "Numerical Simulation of Transient Three-Phase-Systems-Cavitation", ZAMM, Suppl.1, 347–348.

[21] Dickopp Ch., Ballmann J., (2000), "Numerical Simulation of Cavitation Phenomena in Accelerated Liquids", in F. Mayinger, B. Giernoth: Transient Phenomena in Multiphase and Multicomponent Systems, Wiley-VCH, 351–369.

[22] Dilisio R., Grenier E., Pulvirenti M., (1998), "On the convergence of the SPH method", Comp. and Math. Appl., Special Issue devoted to Simulation Method in Kinetic Theory, **35**, 95–108.

[23] Duncan J.H., Zhang S., (1991), "On the interaction of a collapsing bubble and a compliant wall", J. Fluid Mech., **226**, 401–423.

[24] Farhat Ch., Rallu A., Shankaran S., (2008), "A higher-order generalized ghost fluid method for the poor for the three-dimensional two-phase flow computation of underwater implosions", J. Comput. Phys., **227**, No. 16, 7674–7700.

[25] Fedkiw R.P., Aslam T., Marriman B., Osher S., (1999), "A non–oscillatory Eulerian approach to the interfaces in multimaterial flows (the ghost fluid method)", J. Comp. Phys., **152**, 457–492.

[26] Guderley G., (1942), "Starke kugelige und zylindrische Verdichtungsstöße in der Nähe des Kugelmittelpunktes bzw. der Zylinderachse". Luftfahrtforschung, **19**, 302–312.

[27] Hanke M., Ballmann J., (1998), "Strong changes of state in collapsing bubbles", ZAMM, **78**, Suppl. 1, 453–454.

[28] Harten A., Engquist B., Osher S., Chakravarthy S.R., (1987), "Uniformly high order accurate essentially non–oscillatory schemes III", J. Comput. Phys., **71**, 231–303.

[29] Hirt C., Nichols B., (1979), "VOF method for the dynamics of free boundaries", J. Comp. Phys., **39**, 201–225.

[30] Hou G., Wang J., Layton A., (2012), "Numerical methods for fluid-structure interaction - A Review", Commun. Comput. Phys., **12**, No.2, 337–377.

[31] Hurka J., (2002), "Numerische Untersuchung zur Aerolastik dünner Platten", PhD thesis, RWTH Aachen.

[32] Hyman J., (1986), "Moving mesh methods for partial differential equations", Mathematics applied to science, 129–153.

[33] Johnson E., Colonius T., Cleveland R., (2009), "Damage potential of the shock-induced collapse of a gas bubble", in Proceedings of the 7th Int. Symposium on Cavitation CAV2009, Ann Harbor, Michigan, USA, August 17-22, 2009, CAV2009-17.

[34] Kalumuck K.M., Duraiswami R., Chahine G.L., (1995), "Bubble dynamics fluid-structure interaction simulation by coupling fluid BEM and structural FEM codes", J. of Fluids and Structures, **9**, 861–883.

[35] Karni S., (1996), "Hybrid multifluid algorithms", SIAM Journal of Scientific Computing, **17**, 31–43.

[36] Khan A.S., Huang S., (1995), "Continuum Theory of Plasticity", John Wiley & Sons.

[37] Klingenberg Ch., Plohr B., (1996), "An introduction to front tracking", Multidimensional hyperbolic problems and computations, Proc. IMA Workshop, SIAM Journal of Scientific Computing, **17**, 31–43. Minneapolis/MN (USA) 1989, IMA Vol. Math. Appl. 29 (1991), 203–216.

[38] Kröninger D., (2008), "Particle-Tracking-Velocimetry-Messungen an kollabierenden Kavitationsblasen", PhD thesis, Universität Göttingen, `http://webdoc.sub.gwdg.de/diss/2008/kroeninger/`

[39] Lauterborn W., Bolle H., (1975), "Experimental investigations of cavitation-bubble collapse in the neighbourhood of a solid boundary", J. Fluid Mech., **72**, 391-399 (+ two plates facing p. 400).

[40] Lauterborn W., Kurz Th., (2010), "Physics of bubble oscillations", Rep. Prog. Phys., **73**, 106501.

[41] Lemaitre J., (1996), "A Course on Damage Mechanics", Second Edition, Springer Verlag.

[42] Leser H., Wizemann C., Vulcan M., (2004), "Abschlussbericht: Weiterentwicklung und Anwendung der FDEM (Finite Difference Element Method) Programmpaketes zur Lösung partielle Differentialgleichungen", Institut für Umformtechnik, Universität Stuttgart.

[43] Lindau O., Lauterborn W., (2000), "Laser-produced cavitation — Studied with 100 million frames per second", in: Nonlinear Acoustics at the Turn of the Millennium: ISNA15, ed. by W. Lauterborn and T. Kurz, Conference Proceedings Vol. 524, American Institute of Physics, pp. 385-388.

[44] Marshall A. D., (2005), "Programming in C, UNIX System Calls and Subroutines using C", http:www.cs.cf.ac.uk/Dave/C/, 1994-2005.

[45] Massjung R., (2002), "Numerical Schemes and Well-Posedness in Nonlinear Aeroelasticity", PhD thesis, RWTH Aachen.

[46] Mecking K., (2000), "Godunov-Typ Verfahren zur Analyse dynamischer Rißspitzenfelder in elastisch-plastischen Festkörpern mit Materialgrenzen", PhD thesis, RWTH Aachen, Shaker-Verlag.

[47] Monaghan J., (1994), "Simulating free surface flows with SPH", J. Comp. Phys., **110**, 399–406.

[48] Mulder W., Osher S., Sethian J.A., (1992), "Computing interface motion in compressible gas dynamics", J. Comp. Phys., **100**, 209–228.

[49] Müller S., (2003), "Adaptive Multiscale Schemes for Conservation Laws", Lecture Notes in Computational Science and Engineering, Vol. 27, Springer Berlin, 2003.

[50] Müller S., Bachmann M., Kröninger D., Kurz Th., Helluy Ph., (2009), "Comparison and validation of compressible flow simulations of laser-induced cavitation bubbles", Computers & Fluids, **38**, 1850–1862.

[51] Müller S., Helluy Ph., Ballmann J., (2010), "Numerical simulation of a single bubble by compressible two-phase fluids", Int. Journal for Numerical Methods in Fluids, **62**, No. 6, 591–631.

[52] Naudé C.F., Ellis A.T., (1961), "On the mechanism of cavitation damage by nonhemispherical cavities collapsing in contact with a boundary", Trans. ASME D: J. Basic Engng, **83**, 648–656.

[53] Ohl C.D., Ikink R., (2003), "Shock-wave-induced jetting of micron-size bubbles", Phys. Rev. Lett., **90**, 214502-1–4.

[54] Ohl C.-D., Wolfrum B., (2003), "Detachment and sonoporation of adherent HeLa-cells by shock wave-induced cavitation", Biochimia Biophysica Acta, **1624**, 131-138.

[55] Osher S., Fedkiw R.P., (2001), "Level set methods: An overview and some recent results", J. Comp. Phys., **169**, 463–502.

[56] Philipp A., Lauterborn W., (1998), "Cavitation erosion by single laser-produced bubbles", J. Fluid Mech., **361**, 75–116.

[57] Popinet S., Zaleski S., (2002), "Bubble collapse near a solid boundary: A numerical study of the influence of viscosity", J. Fluid Mech., **464**, 137–163.

[58] Rayleigh Lord, (1917), "On the pressure developed in a liquid during the the collapse of a spherical cavity", J. Phil. Mag., **34**, 94–98.

[59] Roe P.L., (1981), "Approximate Riemann solvers, parameter vectors, and difference schemes", J. Comput. Phys., **43**, 357–372.

[60] Saurel R., Abgrall R., (1999), "A simple method for compressible multifluid flows", SIAM J. Sci. Comput., **21**, No. 3, 1115-1145.

[61] Saurel R., Abgrall R., (1999), "A multiphase Godunov method for compressible multiphase flows", J. Comp. Phys., **150**, No. 2, 425–467.

[62] Sethian J.A., (1996), "Level Set Methods", Cambridge Monographs on Applied and Computational Mathematics.

[63] Shutler N.D., Mesler R.B., (1965), "A photographic study of the dynamics and damage capabilities of bubbles collapsing near solid boundaries", Trans. ASME D: J. Basic Eng., **87**, 511–512.

[64] Specht U., (2000), "Numerische Simulation mechanischer Wellen an Fluid-Festkörper-Mediengrenzen", PhD thesis, RWTH Aachen, VDI-Verlag, Reihe 7, Nr. 398.

[65] Turangan C.K., Jamaluddin A.R., Ball G.J., Leighton T.G., (2008), "Free-Lagrange simulations of the expansion and jetting collapse of air bubbles in water", J. Fluid Mech., **598**, 1–25.

[66] Vogel A., Lauterborn W., Timm R., (1989), "Optical and acoustic investigations of the dynamics of laser-produced cavitation bubbles near a solid boundary", J. Fluid Mech., **206**, 299-338.

[67] Voß M., (2002), "Numerische, theoretische und experimentelle Untersuchung zur Kavitationsblasendynamik", PhD thesis, Universität Göttingen.

[68] Wang C.W., Liu T.G., Khoo B.C., (2006), "A real ghost fluid method for the simulation of multimedium compressible flow", SIAM J. Sci. Comput., **28**, No. 1, 278–302.

[69] Welch J., Harlow F., Shannon J., Daly B., (1965), "The MAC method — a computing technique for solving viscous incompressible transient fluid-flow problems involving free surfaces", Report LA-3425, Los Alamos Scientific Laboratory, University of California.

[70] Wulf G., (1992), "Die Berechnung des Implosionsvorgangs in kompressiblen Flüssigkeiten innerhalb abgeschlossener Behälter", PhD thesis, Universität Hannover.

[71] "Elastic Properties and Young Modulus for some materials", http://www.engineeringtoolbox.com/young-modulus-d_417.html.

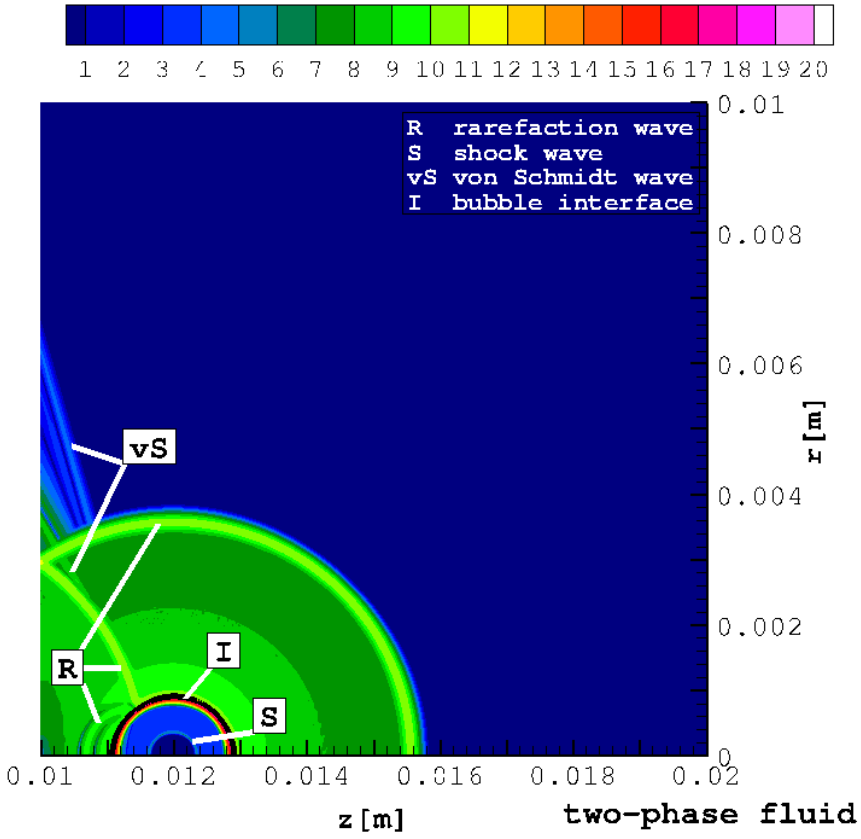

Figure 5: Density gradient magnitude (logarithmic scaling) at $t = 16.6\ \mu$s.

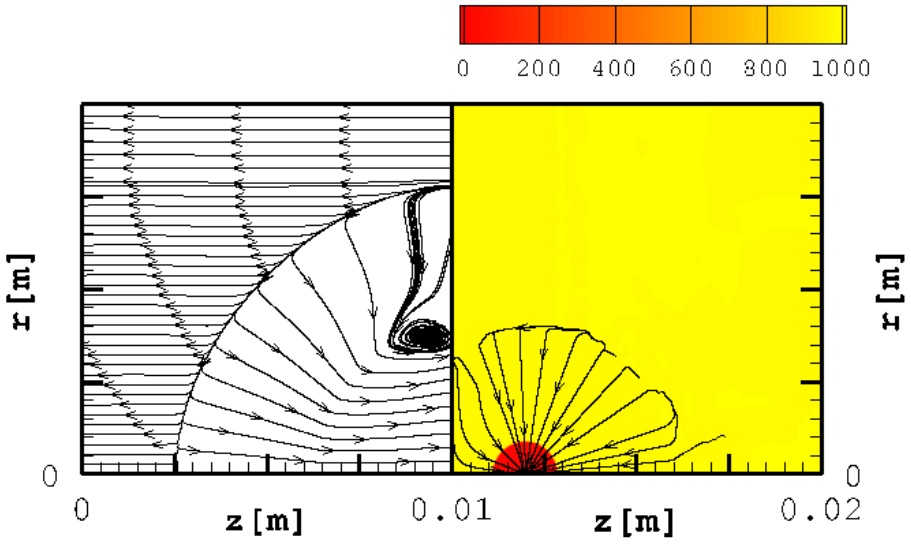

Figure 6: Pathlines in the solid (left) and the fluid (right) and fluid density at $t = 16.6\,\mu s$.

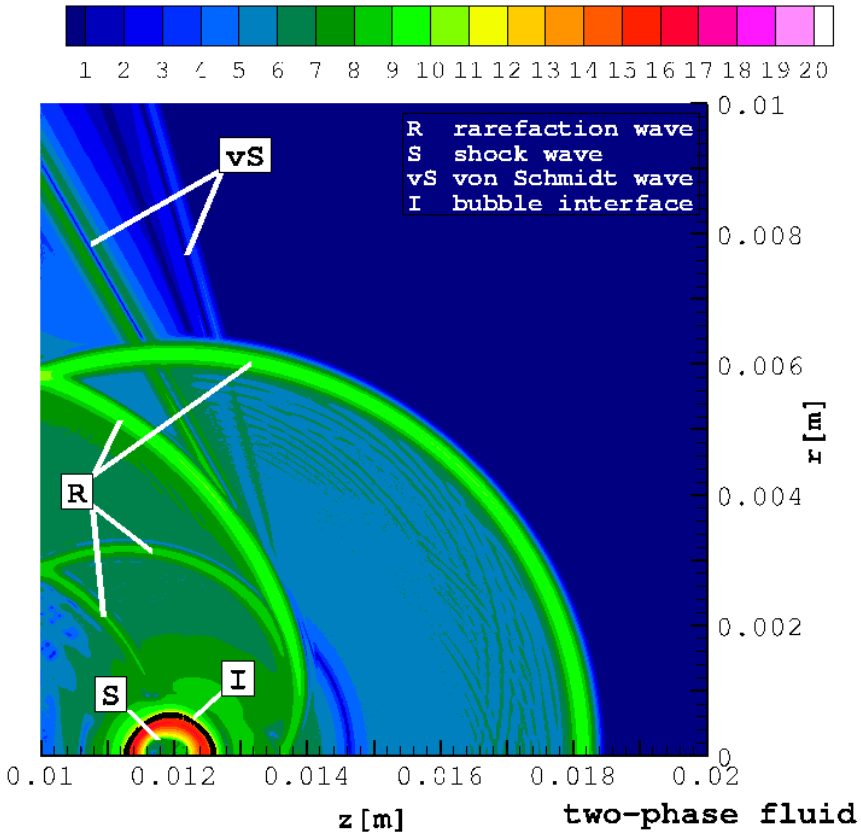

Figure 7: Density gradient magnitude (logarithmic scaling) at $t = 33.1$ μs.

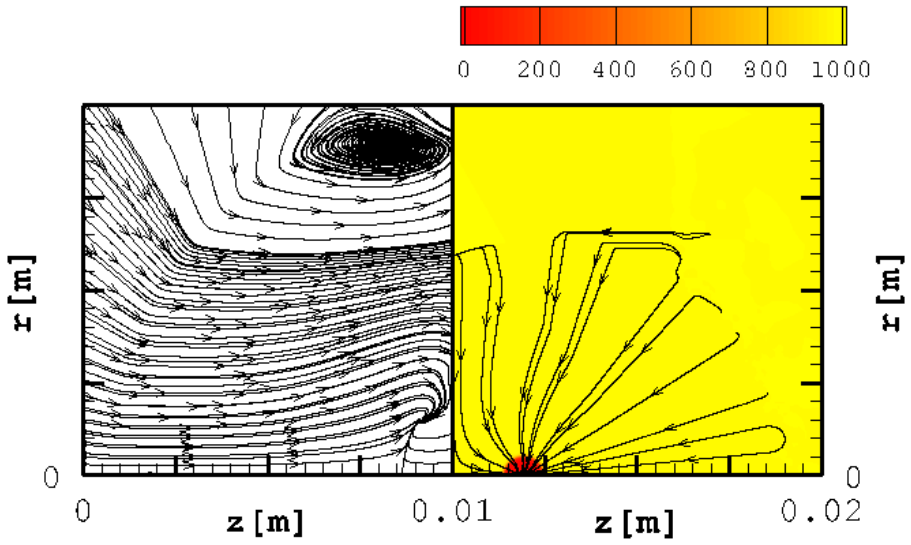

Figure 8: Pathlines in the solid (left) and the fluid (right) and fluid density at $t = 33.1$ μs.

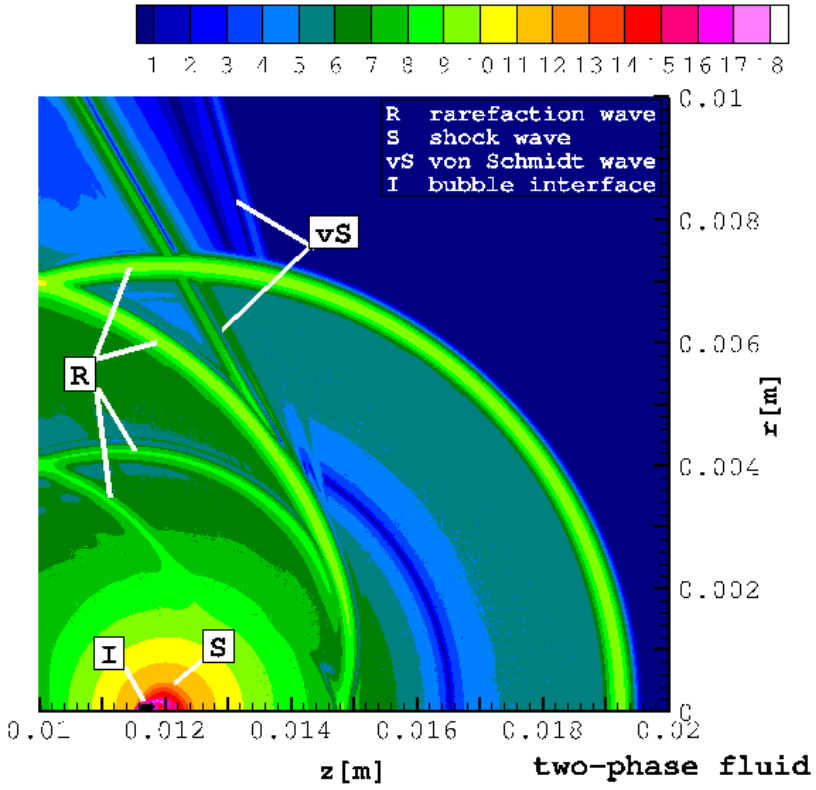

Figure 9: Density gradient magnitude (logarithmic scaling) at $t = 40.0$ μs.

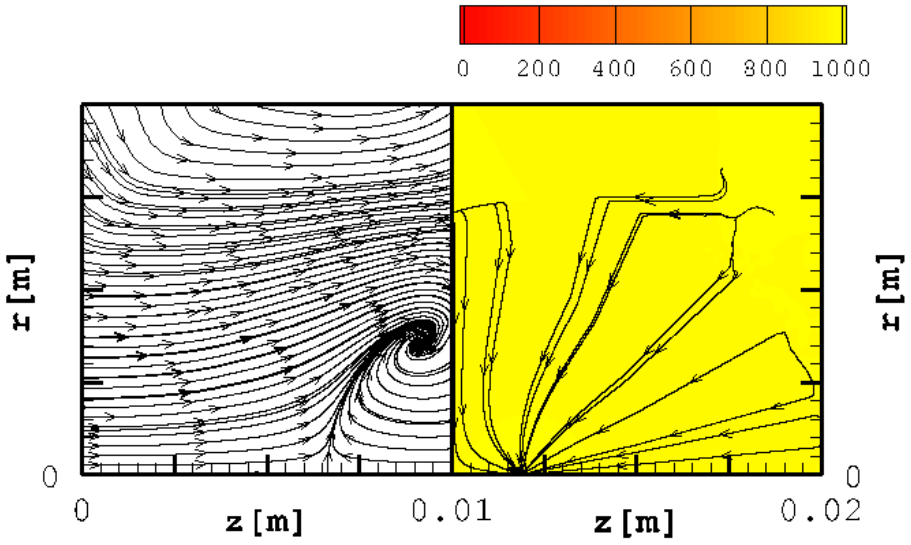

Figure 10: Pathlines in the solid (left) and the fluid (right) and fluid density at $t = 40.0$ μs.

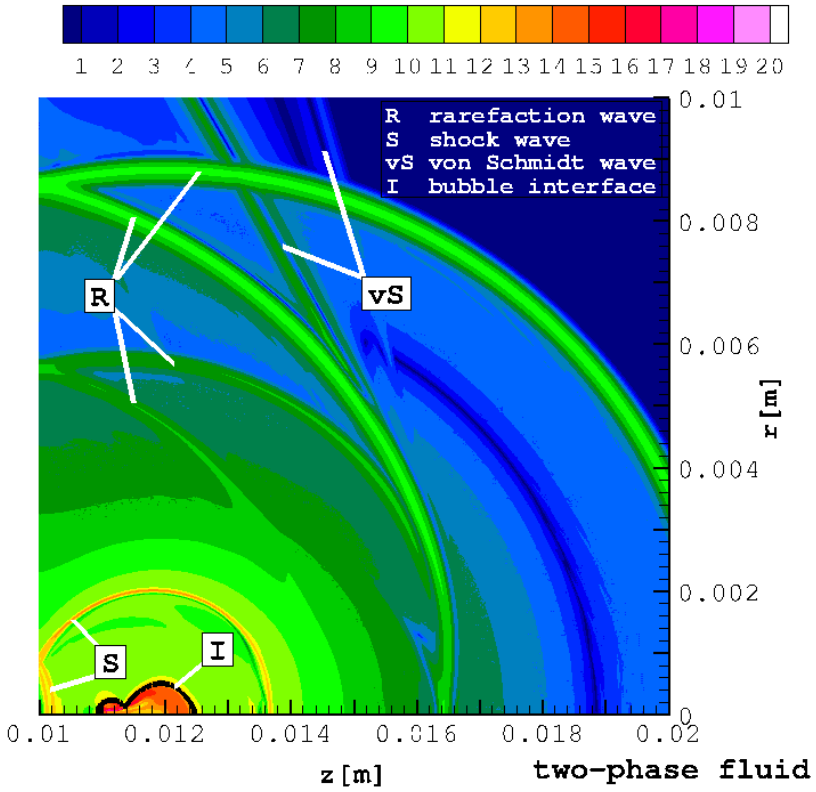

Figure 11: Density gradient magnitude (logarithmic scaling) at $t = 50.0$ μs.

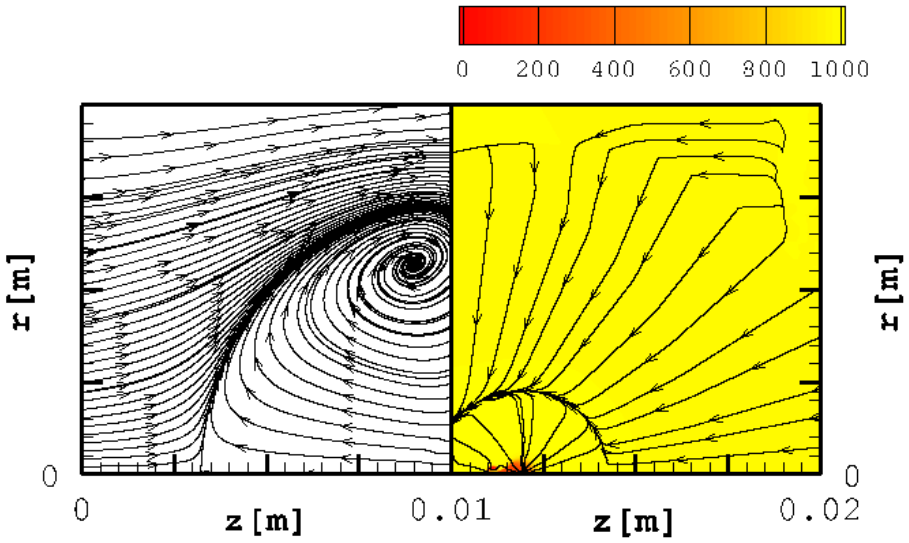

Figure 12: Pathlines in the solid (left) and the fluid (right) and fluid density at $t = 50.0$ μs.

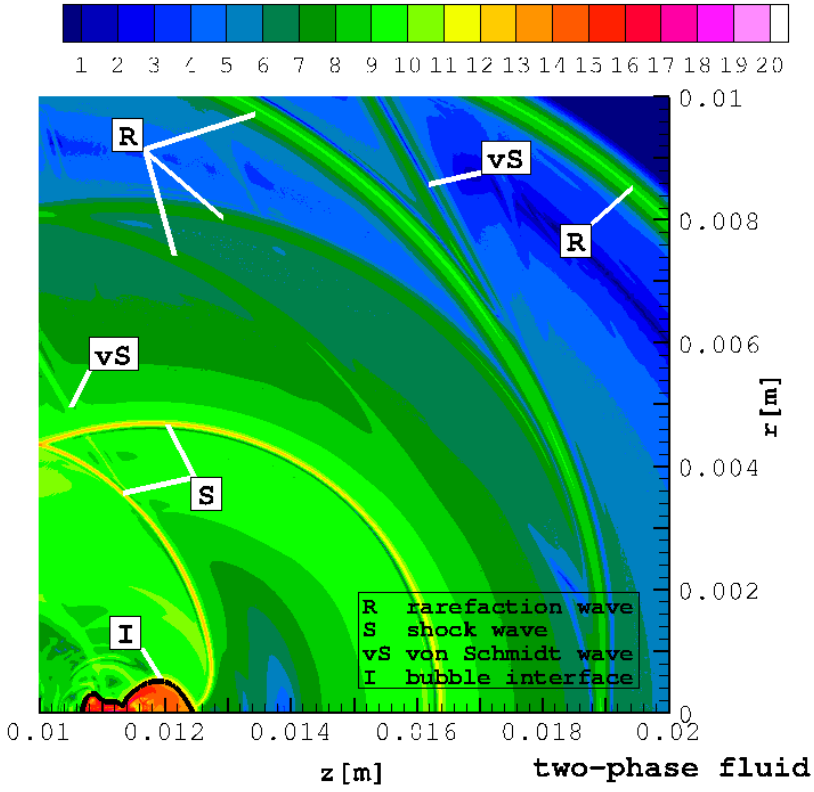

Figure 13: Density gradient magnitude (logarithmic scaling) at $t = 65.7$ μs.

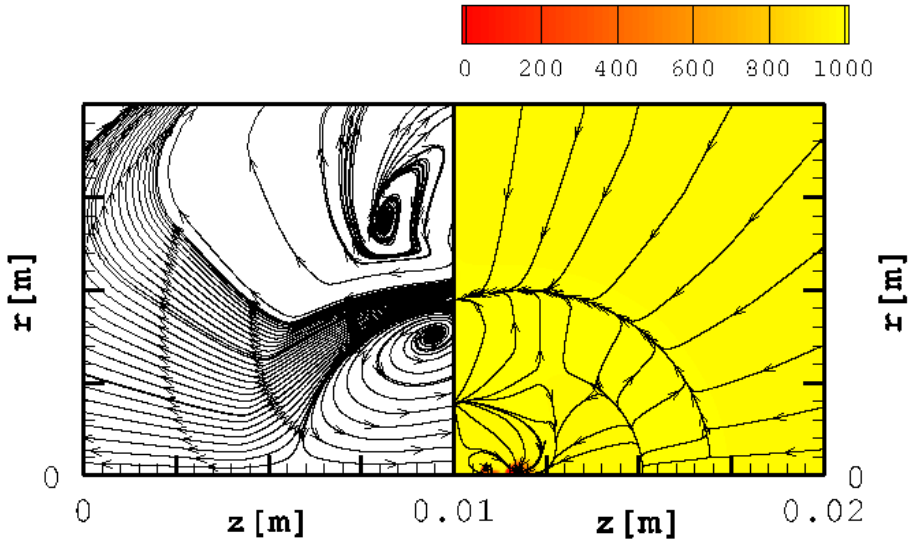

Figure 14: Pathlines in the solid (left) and the fluid (right) and fluid density at $t = 65.7$ μs.

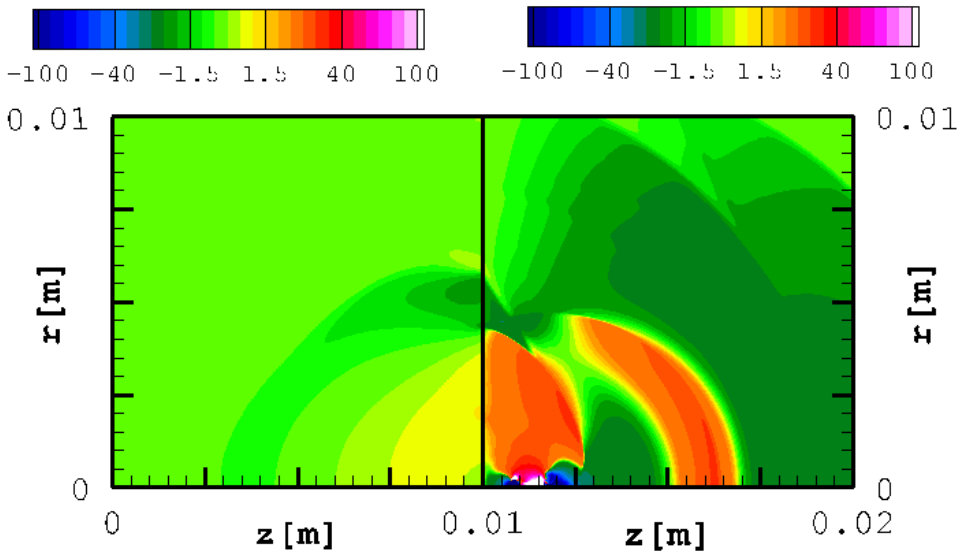

Figure 15: Velocity component v_z in the solid (left) and the fluid (right) at $t = 65.7$ μs.

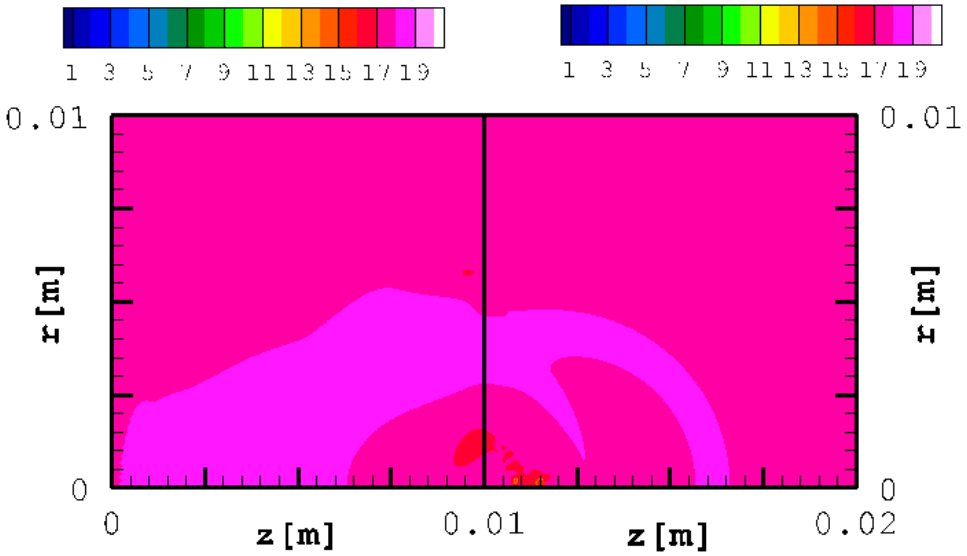

Figure 16: Logarithm of the absolute values of the stress component $\overline{\sigma}_{zz}$ in the solid (left) and the pressure in the fluid (right) at $t = 65.7$ μs.

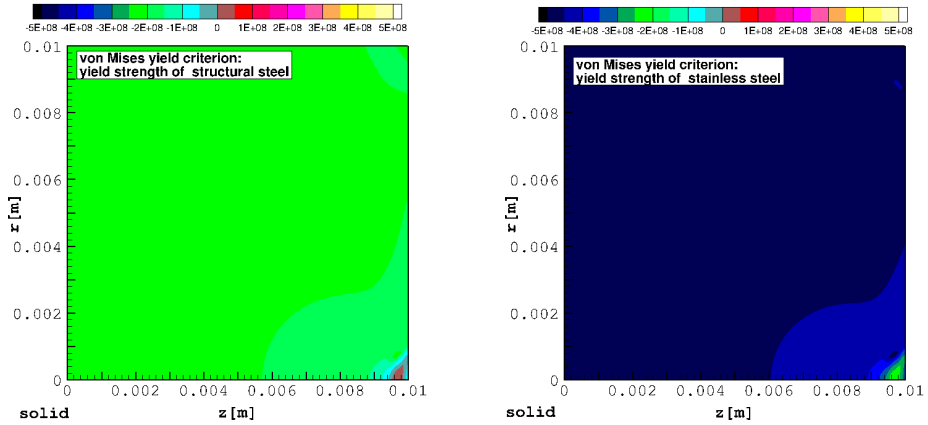

Figure 17: Evaluation of simplified yield criterion for structural steel (left) and stainless steel (right) at $t = 50.0$ μs.

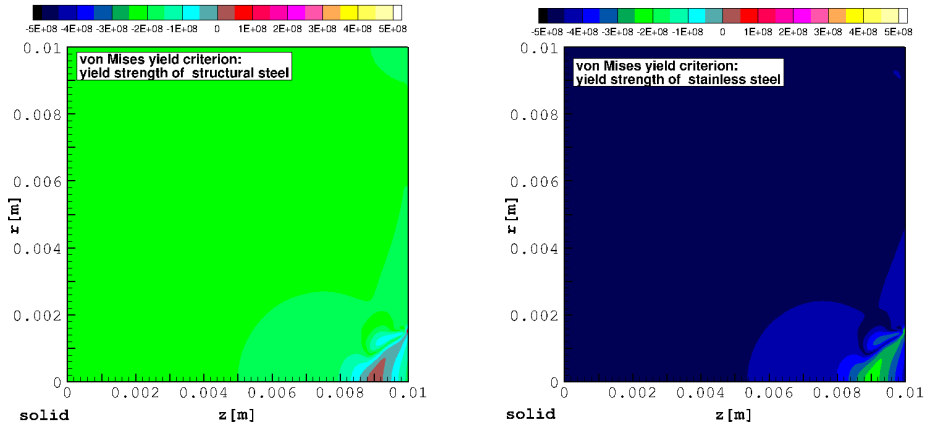

Figure 18: Evaluation of simplified yield criterion for structural steel (left) and stainless steel (right) at $t = 52.0$ μs.

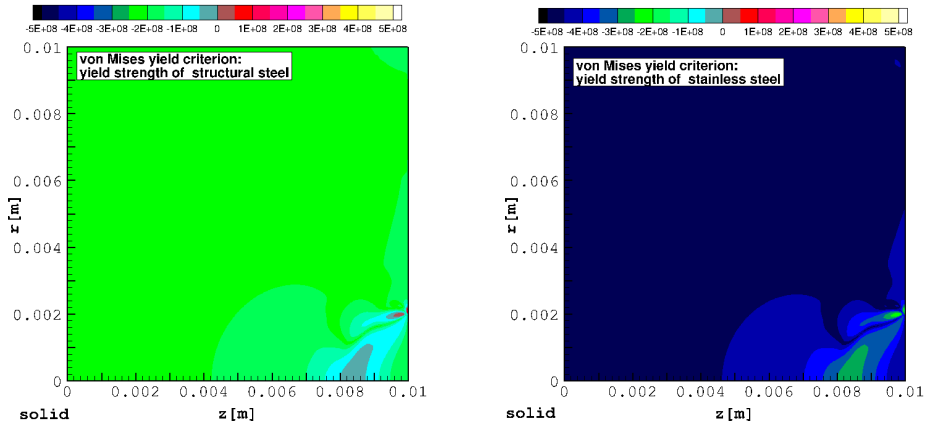

Figure 19: Evaluation of simplified yield criterion for structural steel (left) and stainless steel (right) at $t = 54.0$ μs.

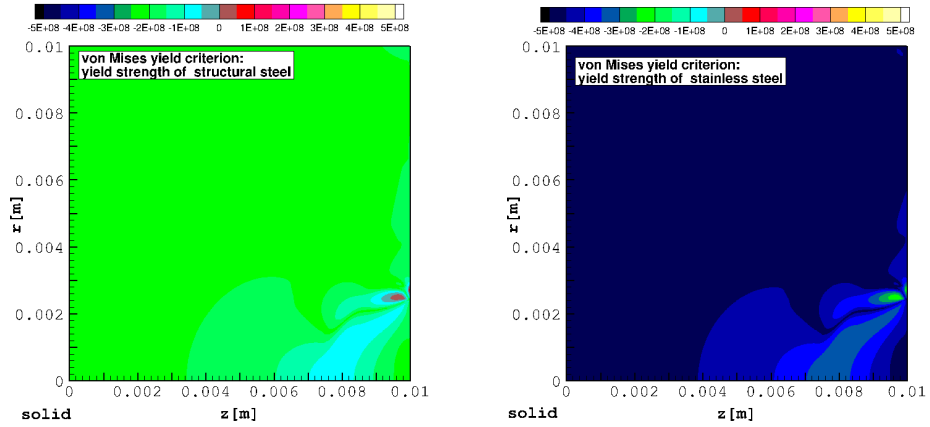

Figure 20: Evaluation of simplified yield criterion for structural steel (left) and stainless steel (right) at $t = 56.0$ μs.

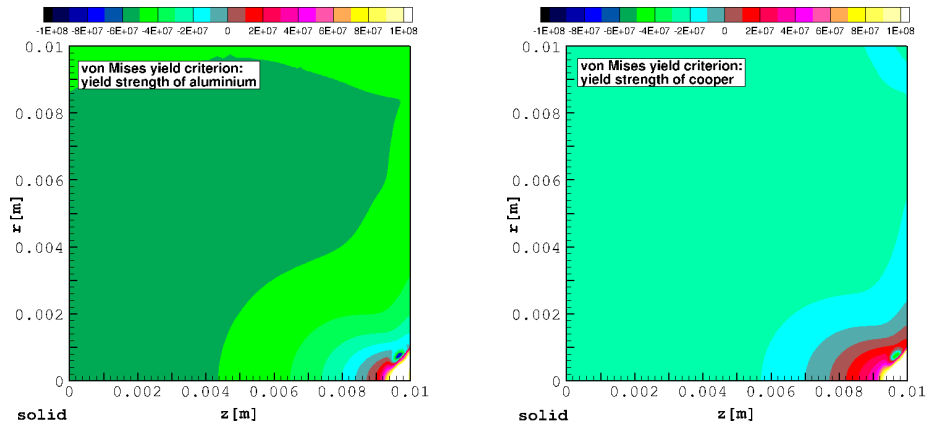

Figure 21: Evaluation of simplified yield criterion for aluminium (left) and copper (right) at $t = 50.0$ μs.